HHS Public Access
Author manuscript
Contrast Media Mol Imaging. Author manuscript; available in PMC 2016 May 01.

Published in final edited form as:
Contrast Media Mol Imaging. 2015 May ; 10(3): 163–178. doi:10.1002/cmmi.1628.

A review of optimization and quantification techniques for chemical exchange saturation transfer (CEST) MRI toward sensitive in vivo imaging

Jinsuh Kim[#1], **Yin Wu**[#2,3], **Yingkun Guo**[3], **Hairong Zheng**[2], and **Phillip Zhe Sun**[3,*]

[1] Department of Radiology, University of Iowa, Iowa City, IA, USA

[2] Paul C. Lauterbur Research Center for Biomedical Imaging, Shenzhen Key Laboratory for MRI, Shenzhen Institutes of Advanced Technology, Chinese Academy of Sciences, Shenzhen, China

[3] Athinoula A. Martinos Center for Biomedical Imaging, Department of Radiology, Massachusetts General Hospital and Harvard Medical School, Charlestown, MA, USA

[#] These authors contributed equally to this work.

Abstract

Chemical exchange saturation transfer (CEST) MRI is a versatile imaging method that probes the chemical exchange between bulk water and exchangeable protons. CEST imaging indirectly detects dilute labile protons via bulk water signal changes following selective saturation of exchangeable protons, which offers substantial sensitivity enhancement and has sparked numerous biomedical applications. Over the past decade, CEST imaging techniques have rapidly evolved due to contributions from multiple domains, including the development of CEST mathematical models, innovative contrast agent designs, sensitive data acquisition schemes, efficient field inhomogeneity correction algorithms, and quantitative CEST (qCEST) analysis. The CEST system that underlies the apparent CEST-weighted effect, however, is complex. The experimentally measurable CEST effect depends not only on parameters such as CEST agent concentration, pH and temperature, but also on relaxation rate, magnetic field strength and more importantly, experimental parameters including repetition time, RF irradiation amplitude and scheme, and image readout. Thorough understanding of the underlying CEST system using qCEST analysis may augment the diagnostic capability of conventional imaging. In this review, we provide a concise explanation of CEST acquisition methods and processing algorithms, including their advantages and limitations, for optimization and quantification of CEST MRI experiments.

1. Introduction

The use of nuclear magnetic resonance (NMR) to detect chemical exchanges originated from the pioneering work of Forsen and Hoffman, who first proposed the double-resonance NMR method for measuring intermediate chemical exchanges (1,2). Their work eventually ushered in the field of chemical exchange saturation transfer (CEST) MRI, a sensitive

[*] Corresponding author: Dr. Phillip Zhe Sun, Ph.D. Athinoula A. Martinos Center for Biomedical Imaging Department of Radiology MGH and Harvard Medical School Rm 2301, 149 13th Street, Charlestown, MA 02129 Phone: 617-726-4060, Fax: 617-726-7422 pzhesun@nmr.mgh.harvard.edu.

method for measuring the chemical exchanges and chemical kinetics of dilute macromolecules (3-9). CEST MRI has shown the ability to detect a variety of compounds (e.g., glucose, glycogen, lactate), proteins and enzymes for molecular imaging (10-24). Development of exogenous CEST agents, including diamagnetic CEST (DIACEST) and paramagnetic CEST (PARACEST) agents, greatly enhanced the sensitivity and specificity of CEST imaging (25-34). In addition, CEST MRI provides a novel imaging approach to track tumor cells, bacterial/viral infections, pH and temperature changes (35-41). Moreover, endogenous CEST effects attributable to labile proton groups from endogenous proteins, peptides and metabolites have been applied to study disorders such as acute stroke, renal injury, tumors and multiple sclerosis (MS) (42-47).

The CEST effect is sensitive to labile proton concentration and exchange rate and, hence, parameters that affect the exchange rate, such as pH and temperature. However, the CEST effect also depends on relaxation rate, magnetic field strength and more importantly, experimental parameters including repetition time, RF irradiation amplitude and scheme, and image readout, which confound CEST measurements (48). Mathematical tools have been established to quantify CEST experiments. With the development of novel CEST agents, it has become increasingly important to optimize CEST experiments for enhanced detectability. Importantly, recent work has demonstrated that the CEST agent concentration and exchange rate can be determined concurrently (49,50). Such advanced post-processing algorithms transform routine CEST-weighted information towards quantitative CEST (qCEST) analysis, which is promising in providing additional insights into underlying biomedical systems (51). Indeed, CEST imaging has seen rapid development due to innovative concepts and improvement in mathematical models, novel contrast agent designs, sensitive data acquisition schemes, post-processing algorithms, and qCEST analysis. Therefore, a comprehensive survey of these new developments is warranted to enhance general understanding of CEST imaging. Herein, we provide a summarized review of the CEST contrast mechanism and methods for optimization and quantification of CEST MRI.

2. Quantitative Description Of CEST MRI

Mathematical models, both numerical and analytical solutions, have been established to describe the CEST contrast mechanism (52-54). A solid mathematical description of the CEST phenomenon is pragmatically useful for optimization and quantification of the CEST effect.

a. Bloch-McConnell solution

The CEST contrast mechanism can be described using Bloch-McConnell equations, which are two sets of Bloch equations coupled by means of chemical exchange. For a typical 2-pool chemical exchange model, assuming the irradiation RF field is applied along the x-axis, we have

$$\begin{aligned}
\frac{dM_x^w}{dt} &= -R_{2w}M_x^w - \Delta\omega_w M_y^w + k_{sw}M_x^s - k_{ws}M_x^w \\
\frac{dM_y^w}{dt} &= \Delta\omega_w M_x^w - R_{2w}M_y^w + k_{sw}M_y^s - k_{ws}M_y^w + \omega_1 M_z^w \\
\frac{dM_z^w}{dt} &= -\omega_1 M_y^w - R_{1w}M_z^w + k_{sw}M_z^s - k_{ws}M_z^w + R_{1w}M_0^w \\
\frac{dM_x^s}{dt} &= -R_{2s}M_x^s - \Delta\omega_s M_y^s + k_{ws}M_x^w - k_{sw}M_x^s \\
\frac{dM_y^s}{dt} &= \Delta\omega_s M_x^s - R_{2s}M_y^s + k_{ws}M_y^w - k_{sw}M_y^s + \omega_1 M_z^s \\
\frac{dM_z^s}{dt} &= -\omega_1 M_y^s - R_{1s}M_z^s + k_{ws}M_z^w - k_{sw}M_z^s + R_{1s}M_0^s
\end{aligned} \quad [1]$$

where $M_0^{w,s}$ are the equilibrium magnetizations for bulk water (w) and solute pool (s); $M_{x,y,z}^{w,s}$ are bulk water and solute magnetizations along x, y and z directions; $R_{1w,s}$ and $R_{2w,s}$ are their longitudinal and transverse relaxation rates, respectively; and k_{sw} and k_{ws} are chemical exchange rates of protons from pool s to pool w and vice versa. In addition, ω_1 is the RF irradiation amplitude, and $\Delta\omega_{w,s}$ is the frequency difference between irradiation RF offset and bulk water, and labile proton chemical shifts, respectively. Bloch-McConnell equations enable not only simulation of CEST experiments but also numerical fitting of CEST measurements (54,55). Furthermore, extended Bloch-McConnell equations that describe multi-pool CEST phenomena can properly take into account concomitant RF irradiation effects, including nuclear overhauser effects (NOE) and magnetization transfer (MT) (56).

b. Modified Bloch-McConnell equations for quantifying the CEST effect

Although the CEST effect is commonly described using the simplistic 2-pool exchange model, CEST systems in reality often involve multiple exchangeable sites (57-59). The extended Bloch-McConnell equations that describe multi-pool CEST systems are mathematically tedious, as the coupling matrix scales with the number of exchangeable sites. To overcome this difficulty, a scalable solution based on the classic 2-pool model has been developed to describe multi-pool CEST phenomena (60). For dilute labile protons that undergo slow or intermediate chemical exchanges, the CEST effect, expressed as CEST ratio (CESTR), can be calculated using the CEST asymmetry analysis as

$$CESTR(\omega_1, \Delta\omega_s) = \frac{I_{ref}(\omega_1, \Delta\omega_s) - I_{label}(\omega_1, \Delta\omega_s)}{I_0} \quad [2]$$

where I_{ref} and I_{label} are the signal intensity with RF irradiation applied at the reference and labile proton frequency, respectively. For well-separated CEST groups, the first order approximation of the CEST effect can be obtained by linear superposition of CESTR for each labile proton group as $CESTR(\omega_1, \Delta\omega) = \sum_i CESTR_i(\omega_1, \Delta\omega_{si})$, where $\Delta\omega_{si}$ is the chemical shift offset of the *i*th labile group.

Incorporation of cross terms that represent the coupling of CEST effects from multiple labile protons yield

$$\begin{aligned}
CESTR(\omega_1, \Delta\omega) \approx & \sum_i CESTR_i(\omega_1, \Delta\omega_{si}) \\
& - \sum_{i>j} \left[\begin{array}{l} CESTR_i(\omega_1, \Delta\omega_s)^* CESTR_j(\omega_1, \Delta\omega_{sj})^* \\ (2 - CESTR_i(\omega_1, \Delta\omega_{si}) - CESTR_j(\omega_1, \Delta\omega_{sj})) \end{array} \right].
\end{aligned} \quad [3]$$

It has been shown that the simplified approach is in good agreement with conventional simulation algorithms and yet expends markedly shorter simulation times. In addition, this simplified approach offers a scalable solution that can be easily expanded using the same simulation routine when CEST systems involve an arbitrary and large number of exchangeable sites.

c. Simplified solution for quantifying the CEST effect

Although numerical methods are useful to quantify CEST phenomena, analytical solutions for CEST imaging can provide further insight into complex CEST effects. Zhou et al. assumed that RF irradiation instantaneously saturates labile protons without direct saturation of bulk water signals, so the Bloch-McConnell equations could be simplified as (53)

$$\begin{aligned}\frac{dM_y^s}{dt} &= \omega_1 m_z^s - r_{2s}M_y^s + k_{ws}M_y^w + \omega_1 M_0^s\\ \frac{dm_z^s}{dt} &= \omega_1 M_y^s - r_{1s}m_z^s + k_{ws}m_z^w\\ \frac{dM_y^w}{dt} &= -r_{2w}M_y^w + k_{SW}M_y^s\\ \frac{dm_z^w}{dt} &= -r_{1w}m_z^w + k_{sw}m_z^s\end{aligned} \quad [4]$$

with $r_{1s,w} = R_{1s,w}+k_{sw,ws}$, $r_{2s,w} = R_{ksw,ws}$, $m_z^s = M_z^s - M_0^s$, and $m_z^w - M_z^w - M_0^w$. The CEST effect can be solved as

$$CESTR = \frac{M_0^w - M_z^w(TS)}{M_0^w} = \frac{f_s \quad k_{sw}}{R_{1w}+f_s \quad k_{sw}}\alpha\left[1 - e^{-(R_{1w}+k_{ws})TS}\right] \quad [5]$$

where TS is the RF saturation time, f_s is labile proton ratio with respect to bulk water, and $\frac{f_s \cdot k_{sw}}{R_{1w}+f_s \cdot k_{sw}}$ is the simplistic CEST solution assuming complete saturation of labile protons without RF spillover effects. Importantly, $\alpha = \frac{\omega_1^2}{\omega_1^2+pq}$ is the saturation efficiency of labile protons (labeling coefficient), where $p = R_{2s}+k_{sw} - \frac{k_{sw}k_{ws}}{R_{2w}+k_{ws}}$ and $q = R_{1s}+k_{sw} - \frac{k_{sw}k_{ws}}{R_{1w}+k_{ws}}$. This equation can adequately describe the CEST effect when assuming negligible direct RF saturation (weak RF irradiation).

d. RF spillover effect-corrected empirical solution for quantifying the CEST effect

The RF spillover effect refers to the concomitant saturation of water protons due to RF irradiation that aims to specifically saturate labile protons. Although Eq. 5 is valid when assuming a weak B_1 field, the concomitant RF spillover effect may not be negligible, particularly in DIACEST MRI experiments where the labile proton chemical shift is in close proximity to that of bulk water resonance (53,61,62). Both labile proton saturation and RF spillover effects are strongly B_1-dependent — the labeling coefficient increases with RF power and so does the concomitant RF spillover effect (63). Therefore, the maximal apparent CEST effect can be achieved at an intermediate RF power level. Sun et al.(63) modified the simplistic solution with a correction of the RF spillover effect as follows:

$$CESTR = \frac{f_s \cdot k_{sw}}{R_{1w}+f_s \cdot k_{sw}} \cdot \alpha \cdot (1-\sigma) \quad [6]$$

where σ is the RF spillover factor, given by

$$\sigma=1-\frac{\mathrm{r_{1w}}}{\mathrm{f_s}\cdot \mathrm{k}_{sw}}\left(\frac{\mathrm{R_{1w}r}_{zs}\,cos^2\,\theta+\mathrm{R_{1s}k}_{ws}\,cos\,\theta\,cos^2\,(\theta/2)}{\mathrm{r}_{zw}\mathrm{r}_{zs}-\mathrm{k}_{ws}\mathrm{k}_{sw}\,cos^2\,(\theta/2)}-\frac{\mathrm{R_{1w}r_{2s}}\,cos^2\,\theta}{\mathrm{r}_{zw}\mathrm{r_{1s}}-\mathrm{k}_{ws}\mathrm{k}_{sw}\,sikn^2\,\theta}\right)\quad [7]$$

in which $\theta=tan^{-1}\left(\frac{\omega_1}{\Delta\omega}\right)$, $r_{ZS} = r_{1s}\cos^2\theta + r_{2s}\sin^2\theta$ $r_{ZW} = r_{1W}\cos^2(\theta/2) + r_{2W}\sin^2(\theta/2)$. It shows that with weak RF power, the spillover factor is negligible (i.e., σ=0), and the modified solution is consistent with that of Zhou et al.

e. Lorentzian fitting for quantifying CEST effects

The Z-spectrum is a plot of the water signal when RF irradiation is swept around the bulk water resonance. For a simplified 3-pool model that includes the CEST effect, direct water saturation (DWS) and macromolecular MT effects, it is reasonable to assume that the concomitant effects are symmetric around the water resonance. A Lorentzian model has been introduced to analyze the combined saturation based on the weak saturation pulse (WSP) approximation (64-66). Lorentzian line shapes for proton transfer ratio (PTR) and DWS are stated as

$$\mathrm{L}\left(\mathrm{A},\Gamma,\Delta\omega\right)=\frac{\mathrm{A}\cdot\Gamma^2/4}{\Gamma^2/4+\Delta\omega^2}\quad [8]$$

with A and Γ being the peak and full width at half maximum (FWHM) of the effect. In addition, the parameters within direct water saturation ($L_0(A0,\Gamma_0)$) and CEST effects ($L_1(A_1,\Gamma_1)$) are

$$\mathrm{A_0}=\frac{\omega_1^2}{\omega_1^2+PQ},\quad \Gamma_0=2\sqrt{\omega_1^2\frac{\mathrm{P}}{\mathrm{Q}}+\mathrm{p}^2},\quad \mathrm{A_1}=\frac{\mathrm{k}_{ws}}{\mathrm{R_{1w}}+\mathrm{k}_{ws}}\frac{\omega_1^2}{\omega_1^2+pq},\quad \Gamma_1=2\sqrt{\omega_1^2\frac{\mathrm{p}}{\mathrm{q}}+\mathrm{p}^2},\quad \text{where}$$
$$\mathrm{P}=\quad \mathrm{R_{2w}}+\mathrm{k}_{ws}-\frac{\mathrm{k}_{ws}\mathrm{k}sw}{\mathrm{R_{2s}}+\mathrm{k}_{sw}},\quad \mathrm{Q}=\mathrm{R_{1w}}+\mathrm{k}_{ws}-\frac{\mathrm{k}_{ws}\mathrm{k}_{sw}}{\mathrm{R_{1s}}+\mathrm{k}_{sw}}.$$

The underlying MT effect can be integrated into the multi-pool approximation function (60), and the combined transfer rate (CTR) is

$$CTR=\frac{\mathrm{L_1}\left(\Delta\omega\right)+\mathrm{L_2}\left(\Delta\omega\right)-2\cdot\mathrm{L_1}\left(\Delta\omega\right)\cdot\mathrm{L_2}\left(\Delta\omega\right)}{1-\mathrm{L_1}\left(\Delta\omega\right)\cdot\mathrm{L_2}\left(\Delta\omega\right)}\quad [9]$$

where L_1 = PTR and L_2 is a Lorentzian function representing MTR'_{asym}. Similarly, Sheth et al. proposed a model function of multiple Lorentzian lines to fit the CEST spectrum as (67)

$$1-\frac{M_s}{M_0}=\frac{A_1 w_1}{\pi\left[(sf-\Delta w_1)^2+w_1^2\right]}+\frac{A_2 w_2}{\pi\left[(sf-\Delta w_2)^2+w_2^2\right]}+\frac{A_3 w_3}{\pi\left[(sf-\Delta w_3)^2+w_3^2\right]}+\frac{A_4}{\pi w_4}\sqrt{\frac{2}{\pi}}\int_0^{\frac{\pi}{2}}\frac{e^{-2\left[\frac{2(sf-\Delta\omega_4)}{w_4|3\cos^2\theta-1|}\right]^2}}{|3\cos^2\theta-1|}\sin\theta d\theta \quad [10]$$

where A, w and Δω are the area, FWHM and center of Lorentzian spectra, respectively. The formula successfully modeled *in vivo* measurement of tumor extracellular pH in conjunction with administration of PARACEST agents (67). Indeed, Desmond et al. constructed endogenous CEST parameter maps of tumor xenografts by decomposing CEST spectra into four Lorentzian line shapes that represent the direct effect, amide, amine, and aliphatic peaks (66).

f. Spin locking theory for quantifying the CEST effect

Quantification of the chemical exchange process using off-resonance spin locking (SL) MRI is shown to be comparable to conventional Z-spectral imaging for slow to intermediate chemical exchanges (68-71). For the classic 2-pool exchange model, the steady-state solution (M_{ss}^{w}) is given as

$$\begin{aligned} M_{ss}^{w} &\approx M_0^{w}\cdot\frac{R_{1w}\cos^2\theta}{R_{1p}} \\ &= M_0^{w}\cdot\frac{R_{1w}\cos^2\theta}{R_{1w}\cos^2\theta+(R_{2w}+k_{sw})\sin^2\theta} \end{aligned} \quad [11]$$

where $R_{1\rho}$ is the longitudinal relaxation rate in the rotating frame. Notably, the CEST effect can be quantified using the inverse difference of the CEST ratio ($CESTR_{ind}$) as follows:

$$\begin{aligned} CESTR_{ind} &= \frac{M_0^{w}}{M_{ss}^{w}(\Delta\omega_s)}-\frac{M_0^{w}}{M_{ss}^{w}(-\Delta\omega_s)} \\ &= \frac{f_s\cdot k_{sw}}{R_{1w}\cos^2\theta}\cdot\alpha \end{aligned} \quad [12]$$

The inverse difference solution of the CEST effect corrects the concomitant RF spillover effect, providing improved quantification of CEST measurement, which is particularly important for DIACEST MRI (72). Note that optimized sensitivity occurs by selecting a moderate RF power, albeit the $CESTR_{ind}$ calculation is immune to RF spillover effects.

3. Dependence Of CEST MRI Measurement

The experimentally measurable CEST effect depends not only on CEST agent concentration and exchange rate, but also on relaxation rate and a number of experimental variables such as field strength, RF irradiation power level and acquisition schemes, including repetition time and flip angle (51). These confounding factors, therefore, need to be carefully examined for qCEST analysis.

a. Relaxation rate

The strong T_1 relaxation rate (T_{1w}) dependence of the CEST effect is explained by the fact that saturation transfer-induced signal reduction is counterbalanced with signal recovery from longitudinal relaxation of the bulk water signal (3). Likewise, the T_2 relaxation rate (T_{2w}) comes into play through the concomitant RF spillover effect (63). Notably, the exchangeable proton pool with a short T_{2w} (i.e., broad spectral width) is exposed to direct RF saturation with the bulk water pool. The empirical solution determining the relationship between the CEST effect and relaxation rates is given in Eq. 7.

b. Magnetic field strength

CEST experiments demonstrate a strong correlation between the CEST effect and field strength through the variability of T_{1w} and $T_{2w,}$ which eventually impacts the spillover effect and the optimal B_1 irradiation level. Figure 1 shows a simulated T_{1w} (Fig. 1a) and T_{2w} (Fig. 1b) for brain gray matter (GM) as a function of field strength (73,74). Simulated CESTR (Eq. 6) of endogenous amide proton transfer ratio (APTR) using an empirical solution demonstrates increasing APTR concomitantly with field strength level that is likely attributable to prolonged T_1 and increased optimal B_1 levels (Fig. 1c). Moreover, APTR initially increases linearly with field strength and gradually plateaus at a very high field regime because the chemical exchange rate of amide protons is relatively slow (Fig. 1d) (42,75). On the other hand, the CEST effect on groups of higher exchange rates, such as amine and hydroxyl groups, significantly increases with field strength.

c. B_1 irradiation level

A lower labeling coefficient from weak RF power (i.e., inefficient labile proton saturation) leads to an attenuated CEST effect. Contrarily, very strong RF power induces a non-negligible RF spillover effect, which is more pronounced in DIACEST MRI where labile proton resonance is in close proximity to that of bulk water. The B_1 dependence of the CEST effect can be described reasonably well with the empirical solution (Eq. 6), which eventually leads to an answer for the optimal RF level that maximizes the CEST effect. Jones et al. (65) investigated the effect of saturation strength and duration on the pulsed steady-state APT effect for a three-compartment model of semisolid macromolecular protons, solute amide protons and bulk water protons. The simulation shows that MTC and DS strongly reduce with B_1 decrease, and a moderate RF irradiation level maximizes APTR by reasonably balancing the labeling coefficient and spillover factor (Fig.2).

d. CEST agent properties

For dilute CEST agents with slow and intermediate chemical exchange rates, the CEST effect approximately linearly correlates with labile proton concentration and exchange rates. However, the CEST effect deviates from the linear relationship when the reverse exchange rate is comparable to the relaxation rate (i.e., $k_{ws}=f_s \cdot k_{sw} \sim R_{1w}$). The equation describes CEST agent kinetics and is analogous to the Michaelis-Menten equation of enzyme kinetics, which can be used to correlate the CEST effect with the concentration of the agent in solution (76). It has been shown that k_{ws} can be estimated and adequately corrected with T_1 normalization (77). Additionally, the relationship between the exchange rate and the CEST effect is complicated by confounding experimental factors, particularly the labeling coefficient and spillover factor that are largely independent of the labile proton fraction ratio (78).

4. Optimization Of CEST MRI Experiments

Optimization of CEST MRI is important particularly in endogenous CEST MRI whose effects are typically small. In this section, we introduce signal-to-noise ratio per unit time (SNR_{put}) for optimizing CEST experiments, as well as experimental parameters that include B_1 level, RF irradiation scheme, repetition time and flip angle.

a. Signal-to-noise ratio efficiency for optimization of CEST MRI

The signal-to-noise ratio (SNR) of the CEST asymmetry effect has been derived as (51)

$$SNR_{CESTR}=\frac{CESTR}{\sqrt{2+CESTR^2}}\cdot SNR_{I_0} \quad [13]$$

where SNR_{I0} is SNR of the control image. This shows that the SNR of CEST imaging varies not only with the magnitude of the CEST effect (i.e., CESTR) but also with SNR_{I0}. Experimental parameters, repetition time, echo time and flip angle are determining factors of SNR_{I0}, which dictate CEST sensitivity. Notably, SNR SNR efficiency (i.e., $SNR_{put}=\frac{SNR_{CESTR}}{\sqrt{TR\cdot NSA}}$) is inversely related with repetition time and number of signal average (NSA). A typical steady-state CEST sequence is comprised of a long RF irradiation module, followed by fast image readout, such as echo planar imaging (EPI), which confers relatively good SNR and spatiotemporal resolution (42,65,71,79,80). Figure 3 shows experimental validation of CEST MRI SNR comparison from an *in vitro* pH phantom. Although the CESTR contrast between two pH compartments (ΔCESTR) steadily increases with TR (Fig. 3a), CNR_{put} (i.e., $CNR_{put}=\frac{CESTR|_{pH(a)}-CESTR|_{pH(b)}}{\sqrt{\left(\sigma^2_{pH(a)}+\sigma^2_{pH(b)}\right)/2}}\cdot\frac{1}{\sqrt{TR\cdot NSA}}$) peaks at an intermediate TR — approximately twice the T_1 (Fig. 3b). Under the optimal TR, we found that both ΔCESTR (Fig. 3a) and CNR_{put} (Fig. 3b) increase with the RF duty cycle. Hence, within the permissible range of scan time and specific absorption rate (SAR) limits, the longest-achievable TS is generally preferred to obtain maximized CEST MRI contrast. Moreover, ΔCESTR decreases with the RF flip angle (Fig. 3a), while CNR_{put} increases with the RF flip angle, which peaks at approximately 75° (Fig. 3b). This result indicates that both the amplitude and SNR efficiency have to be considered when optimizing CEST MRI experiments.

b. Continuous wave (CW) RF irradiation for optimization of CEST MRI

The optimal RF power that maximizes the CEST effect is deduced when the saturation efficiency and spillover factor are balanced (63) as follows:

$$\omega_1=\sqrt{pq}\left\{\sqrt{1+\frac{4\left(\mathrm{f_S}+\mathrm{f_W}\right)\bar{\beta}\,\eta_{2\mathrm{S}}}{\left[\mathrm{f_S}\eta_{2\mathrm{S}}\left(1+2\,\bar{\beta}+\eta_{\mathrm{S}}+4\eta_{\mathrm{W}}\right)+\mathrm{f_W}\left(4+4\beta^2+\eta_{2\mathrm{S}}\left(5+\eta_{2\mathrm{S}}+e\eta_{\mathrm{W}}\right)-4\beta\left(2+\eta_{\mathrm{W}}\right)-4\beta\left(2+\eta_{2\mathrm{S}}+\eta_{2\mathrm{S}}\eta_{\mathrm{W}}\right)\right)\right]}\frac{\Delta\omega^2}{pq}}-1\right\} \quad [14$$

with $\beta=\frac{\mathrm{k}_{WS}\mathrm{k}_{SW}}{\mathrm{r_{1W}r_{1S}}}$, $\bar{\beta}=1-\beta$, $\eta_{\mathrm{W}}=\frac{\mathrm{r_W}}{\mathrm{r_W}}$, $\eta_{\mathrm{S}}=\frac{\mathrm{r_S}}{\mathrm{r_{1S}}}$, $\eta_{2\mathrm{S}}=\frac{\mathrm{r_{2S}}}{\mathrm{r_{1S}}}$, $r_W = r_{2W} - r_{1W}$, $r_S = r_{2S} - r_{1S}$, $\mathrm{f_W}=\frac{\mathrm{R_{1W}}}{\mathrm{r_{1W}}}$ and $\mathrm{f_S}=\frac{\mathrm{R_{1S}}}{\mathrm{k}_{SW}}$. This indicates that the optimal B_1 level depends not only on the labile proton ratio, exchange rate and chemical shift, but also on relaxation rates. Figure 4 shows a numerical simulation of the optimal B_1 irradiation level as a function of field strength and chemical shift when typical T_1 and T_2 values of the GM are assumed (73,74). Note that the "exchange rate normalized" optimal B_1 level (i.e., $\gamma B_1/k_{sw}$) approaches unity at high field and large chemical shift due to a reduced RF spillover effect. At typical clinical field strengths, the optimal RF power level of the DIACEST agents, whose chemical shifts are often less than 5 ppm from the bulk water, is substantially reduced from the exchange rate.

c. Pulsed RF irradiation for optimization of CEST MRI

CEST imaging has been accomplished using long block pulses, a series of short pulses ("pulse train") that has a saturation efficiency similar to that of the long hard pulse, or alternatively steady-state approaches using alternating brief saturation and image acquisition (65). Although the pulse train CEST has been used in some early CEST experiments (42), long continuous-wave (CW) RF irradiation is commonly used in preclinical scanners to establish the steady-state CEST effect prior to image acquisition where the limitations of the RF duty cycle are less of a concern. However, CW irradiation is often not feasible on clinical scanners, which necessitates the use of a pulsed RF or pulse train irradiation scheme (81-84). The pulsed RF irradiation carries at least three parameters to optimize, namely, irradiation pulse duration, flip angle, and inter-pulse delay, in contrast to only one parameter (i.e., B_1) requiring optimization in the case of CW irradiation. Sun et al. investigated the effects of the RF irradiation pulse train and labile proton properties on the pulsed-CEST MRI measurement (82,85), which showed that the optimal pulse irradiation can be reasonably inferred from the well-prescribed CW design. The optimal irradiation flip angle of pulsed irradiation is approximately 180° and is not dependent on acquisition parameters and sample properties. In pulsed-CEST imaging for slow chemical exchange, a flip angle of approximately 180° for each irradiation pulse is suitable because, in this case, an inversion pulse retains labile and bulk water protons in opposite phases. However, the inter-pulse delay of pulsed-CEST MRI degrades saturation efficiency and, hence, measureable CEST effect when imaging intermediate and fast chemical exchanges. In addition, Zu et al. found that the optimal average power and flip angle of pulsed irradiation are independent of each other. Both simulated and experimental results showed the pulsed-CEST contrast peaks at the flip angle of 180°(Fig. 5), and the optimal average power of pulsed irradiation is similar to the optimal RF field amplitude for CW-CEST MRI (86). Schmitt et al. proposed using long-period saturation pulse trains with balanced duty-cycles, which have the advantages of fewer hardware specifications, easy implementation, and low SAR without compromising CEST contrast (87).

PARACEST MRI agents have large chemical shifts, which enable detection of labile protons undergoing a chemical exchange that is faster than DIACEST MRI. However, it requires relatively strong RF irradiation in order to saturate fast labile protons, resulting in an intense SAR. Vinogradov et al. proposed a WALTZ-16 pulse train with amplitude and phase modulation positioned on the bulk water resonance for detection of PARACEST agents that leads to less saturation RF power demand (88). Development of sophisticated on-resonance irradiation pulse schemes with composite pulses can further mitigate the susceptibility to field inhomogeneity for on-resonance CEST imaging schemes. Recently, a time-interleaved parallel transmission based APT-MRI technique using multiple transmission coils has been demonstrated that substantially increased the saturation pulse duration (89).

d. Unevenly-segmented RF irradiation for efficient CEST imaging

Conventional CEST MRI typically consists of a long RF irradiation module followed by fast image acquisition to obtain the steady-state CEST contrast. Because of lengthy RF irradiation and relaxation recovery, it is not efficient to acquire multi-slice CEST images (90). Sun et al. proposed an unevenly segmented RF labeling scheme to enhance CEST imaging sensitivity (91). It includes a long primary RF irradiation sandwiched between a repetitive secondary short RF irradiation module and fast image readout for each saturation block. In this way, the steady-state CEST effect created by the primary irradiation is refreshed by short secondary irradiation during multi-slice excitations, and efficiency of signal acquisition can be significantly improved. This approach clearly demonstrated a significant sensitivity benefit per unit time over the conventional method.

e. Multi-echo CEST MRI for sensitive CEST imaging

For CEST imaging of slow and intermediate chemical exchange, signal averaging is often needed in order to augment CEST sensitivity. Because T_2 signal decay is normalized during the CEST asymmetry calculation, the magnitude of the CEST effect is independent of echo time. It has been shown that a multi-echo EPI readout can yield the same CEST effect as the conventional single-echo acquisition. Moreover, the sensitivity of multi-echo CEST imaging was significantly higher than that of conventional single-echo CEST-EPI acquisition (92). Notably, both SNR and CNR from multi-echo CEST imaging were substantially higher than those obtained by conventional single-echo acquisition, which may facilitate *in vivo* CEST imaging by virtue of substantially improved sensitivity gain.

f. Image readout

There has been a variety of MRI acquisition methods tailored to improve sensitivity and efficiency of CEST imaging. One approach is using a long selective saturation strategy combined with rapid acquisition with relaxation enhancement (RARE) pulse sequences for PARACEST imaging under long T_1 relaxation conditions (93). Alternatively, a fast low-angle shot (FLASH) readout after short selective saturation periods could enhance PARACEST detection under short T_1 relaxation conditions (93). Three-dimensional CEST imaging with gradient- and spin-echo (GRASE) readout that combines the turbo spin-echo (TSE) and EPI along with 2D sensitivity encoding (SENSE) accelerations enabled significant reduction in the CEST acquisition time (94). Recently, Shah et al. integrated the single-shot steady-state free precession (SSFP) readout with CEST RF irradiation, and demonstrated comparable results with EPI readout but with substantially fewer distortion artifacts (95). More recently, keyhole and compressed sensing (CS) CEST MRI have been demonstrated, which may further enhance fast CEST imaging (96-99).

5. Quantitative CEST (qCEST) MRI

The experimentally measured CEST effect involves complex physical and chemical variables, not only parameters of interest such as CEST agent concentration, pH and temperature, but also relaxation rate and other experimental conditions. Development of qCEST analysis is necessary to augment conventional CEST-weighted MRI and to fully characterize the underlying CEST systems (49,50,75,100-102).

a. QUEST and QUESP for quantification of the CEST effect

Equation 5 describes CESTR as a function of saturation RF irradiation time (TS) (53). If T_{1w} can be independently determined, the labile proton ratio-weighted exchange rate can be solved by fitting CESTR as a function of saturation time (i.e., QUEST). This was further simplified with a linear fitting procedure—the reciprocal linear QUEST (RL-QUEST) method (103). In addition, the CEST system can also be quantified by using the RF power dependence of the labeling coefficient (i.e., QUESP). These methods have shown to be successful in determining a self-consistent proton exchange rate. Briefly, QUEST can be more accurate than QUESP owing to the easier measurement of saturation time than that of saturation power, especially with B_1 inhomogeneity, while QUESP has the advantage of not being limited by the demand for precision in labile proton ratio measurement (100). Recently, Randtke et al. developed QUESPT, which measures the CEST effects as a function of saturation time and saturation power, and has the potential to mitigate fitting bias (102). Note that QUEST, QUESP and QUESPT become less effective in quantifying high exchange rate cases due to the overestimation of the saturation efficiency. The Hanes-Woolf linear QUESP (HW-QUESP) method, however, was shown to produce accurate estimates of fast exchange rates because it includes a wide range of saturation power in both the x- and y-values of the plot (102).

b. QUEST with ratiometric analysis (QUESTRA) for improved quantification of the CEST MRI effect

The saturation time-dependent QUEST analysis assumes negligible direct RF saturation. However, it has been shown that a time-dependent CEST effect is governed by $T_{1\rho}$ (longitudinal relaxation rate in the rotating frame), instead of the intrinsic T_1 (68,69). Sun extended the QUEST approach with ratiometric analysis (QUESTRA), which normalizes the magnetization transfer ratio (MTR) at labile frequency by MTR at reference frequency (78)

$$QUESTRA(TS) = \left[1-\left(\frac{MTR_{label}(TS)}{MTR_{lavel\_ss}}\right)\right] / \left[1-\left(\frac{MTR_{ref}(TS)}{MTR_{ref\_ss}}\right)\right] = e^{-f_s \cdot k_{sw} \cdot TS} \quad [15]$$

where MTR_{label_ss} and MTR_{ref_ss} are the steady-state MTR for the label and reference scans, respectively. Because the label and reference scans experience similar direct RF saturation effects, the QUESTRA solution eliminates the confounding spillover effect with little dependence on T_1, T_2, RF irradiation power and chemical shift.

c. RF power-dependent qCEST MRI analysis

Optimization of the B_1-dependent CEST effect has benefited qCEST analysis (63). To account for the semisolid magnetization transfer (MT) effect, a dual 2-pool model was formulated based on the empirical quantitative solution of pH-sensitive *in vivo* APT MRI, which allowed simultaneous determination of labile amide proton concentration and exchange rates at normal and ischemic pH (75). In addition, it has been shown that the optimal RF power, which varies with the exchange rate, has a lesser degree of dependence on the labile proton concentration (50). Under circumstances of multiple RF irradiation levels, the labile proton ratio and exchange rate can be determined independently (49). In addition, Zu et al. resolved the labile proton ratio and exchange rate using the chemical exchange rotation transfer (CERT) approach, which formulates CEST measurement as a function of the flip angle of the irradiation pulse (80,104,105).

d. Omega plot for quantification of the PARACEST MRI effect

Dixon et al. proposed the omega plot for quantifying PARACEST MRI. The labile proton signal intensity is shown to be (106)

$$\frac{\mathrm{M}_{ss}^{\mathrm{w}}}{\mathrm{M}_0^{\mathrm{w}}-\mathrm{M}_{ss}^{\mathrm{w}}}=\frac{\mathrm{k}_{sw}\mathrm{R}_{1\mathrm{w}}}{\mathrm{f}_{\mathrm{s}}}\left(\frac{1}{\mathrm{k}_{sw}^2}+\frac{1}{\omega_1^2}\right) \quad [16]$$

where $\mathrm{M}_{ss}^{\mathrm{w}}$ is steady, the steady-state signal at the labile proton frequency. By plotting $\frac{\mathrm{M}_{ss}^{\mathrm{w}}}{\mathrm{M}_0^{\mathrm{w}}-\mathrm{M}_{ss}^{\mathrm{w}}} vs. \quad 1/\omega_1^2$, the exchange rate can be determined without a priori knowledge of the labile proton ratio and relaxation rate. A phantom study confirmed that the exchange rates estimated from the omega plots were in good agreement with those from the solution of Bloch-McConnell equations at slow exchanging rates. Fast exchanging protons, however, experience incomplete saturation, which introduces measurement inaccuracy. In this case, the Hanes-Woolf QUESP solution may be an alternative approach to minimize such systematic errors (102).

The concomitant RF spillover effect can be corrected to improve the omega plot analysis. It has been shown that the RF spillover effect can be reasonably estimated, and the RF spillover factor-corrected omega plot analysis can be extended for DIACEST MRI as (51,107)

$$\frac{1}{CESTR_\sigma}\approx\left(1+\frac{\mathrm{R}_{1\mathrm{w}}}{\mathrm{f}_{\mathrm{s}}\cdot\mathrm{k}_{sw}}\right)+\frac{\mathrm{k}_{sw}\cdot\left(\mathrm{R}_{2\mathrm{s}}+\mathrm{k}_{sw}\right)\left(1-\frac{\mathrm{f}_{\mathrm{s}}\cdot\mathrm{k}_{sw}}{\mathrm{R}_{1\mathrm{w}}+\mathrm{f}_{\mathrm{s}}\cdot\mathrm{k}_{sw}}\right)\left(1+\frac{\mathrm{R}_{1\mathrm{w}}}{\mathrm{f}_{\mathrm{s}}\cdot\mathrm{k}_{sw}}\right)}{\omega_1^2}. \quad [17]$$

Both the labile proton exchange rate and ratio can be solved with $\mathrm{k}_{sw}=\frac{\sqrt{\mathrm{R}_{2\mathrm{s}}^2+4\cdot\mathrm{C}_1/\left(\mathrm{C}_0-1\right)}-\mathrm{R}_{2\mathrm{s}}}{2}$ and $\mathrm{f}_{\mathrm{s}}=\frac{\mathrm{R}_{1\mathrm{w}}}{\mathrm{k}_{sw}\cdot\left(\mathrm{C}_0-1\right)}$, where C_0 and C_1 are the intercept and slope of the modified omega plot analysis.

e. Ratiometric pH MRI

The ratiometric CEST MRI compares the CEST effects from multiple labile protons of the same molecule. The normalization calculation makes the ratiometric measurement independent of CEST agent concentration, resulting in substantial simplification of qCEST analysis (108,109). Sheth et al. investigated a PARACEST contrast agent (Yb-DO3A-oAA) to measure extracellular pH (67,110). Figure 6 shows excellent linearity between the CEST effects, and the pH exhibited good dynamic range (67). Recently, iopamidol, a food and drug administration (FDA)-approved CT contrast agent, has demonstrated potential for pH imaging (111). Longo et al. demonstrated that iopamidol pH MRI can monitor renal pH changes in acute renal injury (112,113). Alternative iodinated CT agents (iopromide) for pH imaging have also been evaluated (114). More recently, a method for endogenous ratiometric CEST MRI has been developed for *in vivo* pH imaging by comparing amide and amine exchangeable groups (66,115).

6. Artifacts And Post-Processing

Because the CEST effect is typically small, CEST MRI is prone to field inhomogeneity artifacts. In addition, conventional asymmetry analysis is subject to lipid signal contamination and contributions from asymmetric MT and NOE, which have to be considered when measuring the *in vivo* CEST effect.

a. Field inhomogeneity

The CEST effect is sensitive to field inhomogeneity (116-121). B_0 inhomogeneity can be measured using a conventional field map (122). B_0 shift can also be determined by fitting the direct water saturation with Bloch-McConnell (77) or Lorentzian line models (64,65,123), or a water saturation shift referencing the (WASSR) approach (122,124,125). B_0 inhomogeneity-induced CEST artifacts can be corrected by aligning the interpolated Z-spectrum based on B_0 shift. WASSR correction can be achieved with partial Z-spectral sampling in segments around the label and reference frequencies to shorten the scan time (84,126). Moreover, B_0 inhomogeneity correction can also be rectified with a model-based algorithm. Sun et al. showed that the MT asymmetry calculation is given by (75)

$$MTR_{asym}=CESTR^{'}+\Delta MTR \quad [19]$$

where CESTR′ represents CESTR with B_0 field inhomogeneity contamination, and ΔMTR is the MTR offset due to a field inhomogeneity-induced MTR shift. Taking into account field inhomogeneity-modulated experimental factors, the corrected PTR can be shown to be CESTR = η · CESTR′ = η ·(MTR_{asym} − ΔMTR), where η is the modulation factor: $\eta=\frac{\alpha(\mathrm{B}_1,\Delta\omega_\mathrm{s})\cdot(1-\sigma(\mathrm{B}_1,\Delta\omega_\mathrm{s}))}{\alpha(\mathrm{B}_1,\Delta\omega_\mathrm{s}+\Delta\omega)\cdot(1-\sigma(\mathrm{B}_1,\Delta\omega_\mathrm{s}+\Delta\omega))}$. The compensated CESTR is given as

$$CESTR=\frac{\alpha(\mathrm{B}_1,\Delta\omega_\mathrm{s})\cdot(1-\sigma(\mathrm{B}_1,\Delta\omega_\mathrm{s}))}{\alpha(\mathrm{B}_1,\Delta\omega_\mathrm{s}+\Delta\omega)\cdot(1-\sigma(\mathrm{B}_1,\Delta\omega_\mathrm{s}+\Delta\omega))} \times\left[MTR_{asym}-\frac{4\Delta\omega_\mathrm{s}\omega_1^2\mathrm{T}_{1\mathrm{w}}\mathrm{T}_{2\mathrm{w}}^3\Delta\omega}{\left(1+\Delta\omega_{ref}^2\mathrm{T}_{2\mathrm{w}}^2+\omega_1^2\mathrm{T}_{1\mathrm{w}}\mathrm{T}_{2\mathrm{w}}\right)\left(1+\Delta\omega_{lavel}^2\mathrm{T}_{2\mathrm{w}}^2+\omega_1^2\mathrm{T}_{1\mathrm{w}}\mathrm{T}_{2\mathrm{w}}\right)}\right]. \quad [20]$$

Recently, Song et al. proposed a new CEST phase mapping scheme based on length and offset varied saturation (LOVARS). Figure 7 displays the LOVARS scheme as applied to the imaging of 9L gliosarcomas in mice. The WASSR map (Fig. 7b) shows substantial B_0 variation, which distorts the MTR_{asym} map (Fig. 7c). The LOVARS phases show a large difference between the two ROIs (Fig. 7d), despite their similar MTR_{asym} magnitudes in the uncorrected CEST map (Fig. 7c). With either fast Fourier transform (FFT) (Fig. 7e) or the general linear model (GLM) (Fig. 7f), the thresholded imaginary component map (Fig. 7g) contains the same information as that obtained by conventional MTR_{asym} correction, but with the superiority of higher CNR and less sensitivity to field inhomogeneity (127).

b. Filtering of CEST MRI

To improve quantitative interpretation of CEST contrast maps, Liu et al. proposed an MRI segmentation technique based on two resonance frequency offsets and the normalized magnetization ratio (NOMAR) filtering, which is defined as (128)

$$NOMAR\left(\Delta\omega_1/\Delta\omega_2\right)=\frac{1-MTR\left(\Delta\omega_1\right)}{1-MTR\left(\Delta\omega_2\right)}. \quad [18]$$

c. Lipid Artifacts

Amide proton transfer (APT) imaging is a specific form of CEST imaging that probes amide protons from endogenous proteins/peptides. Because the lipid chemical shift (-3.5 ppm) is situated approximately equal to the reference frequency for endogenous amide protons (3.5 ppm), conventional asymmetry analysis is prone to lipid contamination. This lipid artifact is particularly prominent in the CEST-EPI sequence due to a chemical shift-induced pixel change along the phase encoding direction. Sun et al. developed a lipid signal suppression method using a chemical shift-selective refocusing pulse (129). For multi-slice acquisition, a fat suppression pulse should be positioned immediately prior to the EPI readout to minimize lipid contamination (91). Notably, although a lipid-induced voxel shift is less problematic in non-EPI-based sequences due to higher phase encoding bandwidth, lipid suppression is still important to distinguish confounding asymmetric saturation transfer effects, such as NOE from lipids (130).

d. Quantitative *in vivo* CEST MRI

In vivo CEST MRI has been applied to study a number of disorders, including acute stroke, tumors, MS, and renal injury (22,43,123,131-136). However, endogenous APT MRI can be confounded by concomitant T_1, T_2, MT and NOE changes, and *in vivo* qCEST MRI provides important diagnostic value (137-142).

Because T_1, T_2 and semisolid MT changes during acute stroke are relatively small, *in vivo* qCEST MRI analysis has been applied to quantify tissue acidosis during acute stroke (143-145). Reasonably homogeneous labeling coefficient and spillover factor maps were calculated from an empirical solution (Eq. 6). Note that the *in vivo* MTR_{asym} is negative due to the baseline shift of the $\Delta MTR'_{asym}$. The routine pH-weighted MTR_{asym} map shows significant regional differences between cerebral WM and GM that is attributable to the concomitant RF irradiation effects and does not reflect pH. However, the tissue pH map derived from qCEST analysis accurately represents tissue acidification in the ischemic lesion. Recently, Zaiss et al. proposed an MT ratio (MTR_{Rex}) analysis using the inverse Z-spectrum to eliminate spillover and semisolid MT effects (72). Conventional APT contrast (Fig. 8a) is contaminated by DS and T_1 effects (Figs. 8d, e). By correcting the spillover with MTR_{Rex} (Fig. 8b), and correcting the T_1 using the apparent exchange-dependent relaxation (AREX) evaluation (Fig. 8c), a pH map can be calculated (Fig. 8f) that will show significantly improved contrast between ischemic and normal regions (Fig. 8g).

7. Conclusion

CEST MRI is a sensitive imaging method that can characterize the chemical and biological properties of intracellular and extracellular domains of the tissue. However, the conventional CEST-weighted MRI method is limited by its dependence on experimental conditions. The emerging qCEST analysis method enables simultaneous determination of labile proton ratio and exchange rate, and is expected to provide an invaluable paradigm for *in vivo* imaging. Along with innovative acquisition, optimization and quantification methods, CEST MRI opens the way to an unbiased measure of important biological information for clinical translation.

Acknowledgements

This study was supported in part by grants from China Scholarship Council (Drs. Wu and Guo), NSFC 81120108012 (Dr. Wu), NIH/NIBIB 1K01EB009771 (Dr. Sun) and NIH/NINDS 1R01NS083654 (Dr. Sun). The authors wish to thank Ms. Nichole Jenkins for editorial assistance.

Table of abbreviations

APT(R)	Amide Proton Transfer (Ratio)
AREX	Apparent Exchange-dependent Relaxation
CERT	Chemical Exchange Rotation Transfer
CEST(R)	Chemical Exchange Saturation Transfer (Ratio)
qCEST	Quantitative CEST
CNR	Contrast-to-Noise Ratio
CS	Compressed Sensing
CTR	Combined Transfer Rate
CW	Continuous Wave
DIACEST	Diamagnetic CEST
D(W)S	Direct Water Saturation
EPI	Echo Planar Imaging
FFT	Fast Fourier Transform
FISP	Fast Imaging with Steady Precession

FLASH	Fast Low-angle SHot
FWHM	Full Width at Half Maximum
GLM	General Linear Model
GM	Gray Matter
GRASE	Gradient And Spin-Echo
LOVARS	Length and Offset VARied saturation
MT(R)	Magnetization Transfer (Ratio)
MTR_{asym}	Magnetization Transfer Ratio Asymmetry
MTR_{Rex}	Spillover-correct Magnetization Transfer Ratio Yielding R_{ex}
NOE	Nuclear Overhauser Effect
NOMAR	NOrmalized MAgnetization Ratio
NSA	Number of Signal Average
PARACEST	Paramagnetic CEST
PTR	Proton Transfer Rate
QUESP	QUantification of Exchange as a function of Saturation Power
QUEST(RA)	QUantification of Exchange as a function of Saturation Time (Ratiometric Analysis)
RARE	Rapid Acquisition with Relaxation Enhancement
rCEST(R)	Ratiometric CESTR (Ratio)
RF	RadioFrequency
RL-QUEST	Reciprocal Linear-QUEST
SAR	Specific Absorption Rate
SENSE	SENSitivity Encoding
SL	Spin Locking
SNR_{put}	Signal-to-Noise Ratio per unit time
SSFP	Steady-State Free Precession
TE	Echo Time
TR	Repetition Time
TS	Saturation RF irradiation time
TSE	Turbo Spin-Echo
WASSR	WAter Saturation Shift Referencing
WSP	Weak Saturation Pulse

Table of mathematical notations

A, Γ	Peak and full width half maximum (FWHM) of a Lorentzian line shape
α	Labeling coefficient or excitation pulse flip angle
CESTR′	CESTR with B_0 field inhomogeneity contamination
ΔMTR	MTR offset due to a field inhomogeneity-induced MTR shift
$\Delta\omega_{w,s}$	Frequency difference between the labeling RF and the labile proton resonance
η	Field inhomogeneity-modulated experimental factor of CESTR
Ω	Frequency offset of spin-lock pulse
f_s	Labile proton concentration with respect to bulk water
γ	Gyromagnetic ratio
I_{ref}, I_{label}	Image intensity with RF irradiation applied at the reference and labile proton frequency
k_{sw}, k_{ws}	Chemical exchange rate of protons, from pool s (w) to pool w (s)
L_1	Proton transfer rate
L_2	Lorentzian function representing MTR'_{asym}
$M_0^{w,s}$	Equilibrium magnetizations for bulk water (w) and solute pool (s)
$M_{x,y,z}^{w,s}$	Bulk water and solute magnetizations along x, y and z directions
M_{ss}^{w}	Steady-state signal at the labile proton frequency
$R_{1w,s}$, $R_{2w,s}$	Longitudinal and transverse relaxation rates of bulk water and labile groups
$R_{1\rho}$	Longitudinal relaxation rate in the rotating frame
R_{ex}	Chemical exchange relaxation rate
σ	Spillover factor
T_{1w}	Longitudinal relaxation rate of water proton
$T_{1\rho}$	T_1 relaxation time in the rotating frame
T_{2w}	Transverse relaxation rate of water proton
Θ	Lock angle of the water magnetization
ω_1	Irradiation RF power

References

1. Forsen S, Hoffman RA. Study of moderately rapid chemical exchange reactions by means of nuclear magnetic double resonance. J Chem Phys. 1963; 39:2892–2901.
2. Bain AD. Chemical exchange in NMR. Prog Nucl Mag Reson Spectrosc. 2003; 43(3):63–103.
3. Ward KM, Aletras AH, Balaban RS. A new class of contrast agents for MRI based on proton chemical exchange dependent saturation transfer (CEST). J Magn Reson. 2000; 143:79–87. [PubMed: 10698648]

4. Liu G, Song X, Chan KWY, McMahon MT. Nuts and bolts of chemical exchange saturation transfer MRI. NMR Biomed. 2013; 26(7):810–828. [PubMed: 23303716]
5. van Zijl PCM, Yadav NN. Chemical exchange saturation transfer (CEST): What is in a name and what isn't? Magn Reson Med. 2011; 65(4):927–948. [PubMed: 21337419]
6. Terreno E, Castelli D, Aime S. Encoding the frequency dependence in MRI contrast media: the emerging class of CEST agents. Contrast Media Mol Imaging. 2010; 5(2):78–98. [PubMed: 20419761]
7. Vinogradov E, Sherry AD, Lenkinski RE. CEST: From basic principles to applications, challenges and opportunities. J Magn Reson. 2013; 229(0):155–172. [PubMed: 23273841]
8. Sherry AD, Woods M. Chemical exchange saturation transfer contrast agents for magnetic resonance imaging. Annu Rev Biomed Eng. 2008; 10:391–411. [PubMed: 18647117]
9. Zaiss M, Bachert P. Chemical exchange saturation transfer (CEST) and MR Z-spectroscopy in vivo: a review of theoretical approaches and methods. Phys Med Biol. 2013; 58(22):221–269.
10. Aime S, Delli Castelli D, Fedeli F, Terreno E. A paramagnetic MRI-CEST agent responsive to lactate concentration. J Am Chem Soc. 2002; 124(32):9364–9365. [PubMed: 12167018]
11. Zhang S, Trokowski R, Sherry AD. A paramagnetic CEST agent for imaging glucose by MRI. J Am Chem Soc. 2003; 125(50):15288–15289. [PubMed: 14664562]
12. Winter PM, Cai K, Chen J, Adair CR, Kiefer GE, Athey PS, Gaffney PJ, Buff CE, Robertson JD, Caruthers SD, Wickline SA, Lanza GM. Targeted PARACEST nanoparticle contrast agent for the detection of fibrin. Magn Reson Med. 2006; 56(6):1384–1388. [PubMed: 17089356]
13. van Zijl PCM, Jones CK, Ren J, Malloy CR, Sherry AD. MRI detection of glycogen in vivo by using chemical exchange saturation transfer imaging (glycoCEST). Proc Natl Acad Sci U S A. 2007; 104(11):4359–4364. [PubMed: 17360529]
14. Liu G, Li Y, Pagel MD. Design and characterization of a new irreversible responsive PARACEST MRI contrast agent that detects nitric oxide. Magn Reson Med. 2007; 58(6):1249–1256. [PubMed: 18046705]
15. Ling W, Regatte RR, Navon G, Jerschow A. Assessment of glycosaminoglycan concentration in vivo by chemical exchange-dependent saturation transfer (gagCEST). Proc Natl Acad Sci U S A.
16. Liu G, Liang Y, Bar-Shir A, Chan KWY, Galpoththawela CS, Bernard SM, Tse T, Yadav NN, Walczak P, McMahon MT, Bulte JWM, van Zijl PCM, Gilad AA. Monitoring Enzyme Activity Using a Diamagnetic Chemical Exchange Saturation Transfer Magnetic Resonance Imaging Contrast Agent. J Am Chem Soc. 2011; 133(41):16326–16329. [PubMed: 21919523]
17. Cai K, Haris M, Singh A, Kogan F, Greenberg JH, Hariharan H, Detre JA, Reddy R. Magnetic resonance imaging of glutamate. Nat Med. 2012; 18(2):302–306. [PubMed: 22270722]
18. Singh A, Haris M, Cai K, Kassey VB, Kogan F, Reddy D, Hariharan H, Reddy R. Chemical exchange saturation transfer magnetic resonance imaging of human knee cartilage at 3 T and 7 T. Magn Reson Med. 2012; 68(2):588–594. [PubMed: 22213239]
19. Hingorani DV, Randtke EA, Pagel MD. A CatalyCEST MRI Contrast Agent That Detects the Enzyme-Catalyzed Creation of a Covalent Bond. J Am Chem Soc. 2013; 135(17):6396–6398. [PubMed: 23601132]
20. Nasrallah FA, Pages G, Kuchel PW, Golay X, Chuang K-H. Imaging brain deoxyglucose uptake and metabolism by glucoCEST MRI. J Cereb Blood Flow Metab. 2013; 33(8):1270–1278. [PubMed: 23673434]
21. Walker-Samuel S, Ramasawmy R, Torrealdea F, Rega M, Rajkumar V, Johnson SP, Richardson S, Goncalves M, Parkes HG, Arstad E, Thomas DL, Pedley RB, Lythgoe MF, Golay X. In vivo imaging of glucose uptake and metabolism in tumors. Nat Med. 2013; 19(8):1067–1072. [PubMed: 23832090]
22. Kogan F, Haris M, Singh A, Cai K, Debrosse C, Nanga RPR, Hariharan H, Reddy R. Method for high-resolution imaging of creatine in vivo using chemical exchange saturation transfer. Magn Reson Med. 2014; 71(1):164–172. [PubMed: 23412909]
23. Yoo B, Sheth VR, Howison CM, Douglas MJK, Pineda CT, Maine EA, Baker AF, Pagel MD. Detection of in vivo enzyme activity with CatalyCEST MRI. Magn Reson Med. 2014; 71(3): 1221–1230. [PubMed: 23640714]

24. Longo DL, Di Gregorio E, Abategiovanni R, Ceccon A, Assfalg M, Molinari H, Aime S. Chemical exchange saturation transfer (CEST): an efficient tool for detecting molecular information on proteins' behaviour. Analyst. 2014; 139(11):2687–2690. [PubMed: 24733370]

25. Aime S, Barge A, Delli Castelli D, Fedeli F, Mortillaro A, Nielsen FU, Terreno E. Paramagnetic Lanthanide(III) complexes as pH-sensitive chemical exchange saturation transfer (CEST) contrast agents for MRI applications. Magn Reson Med. 2002; 47:639–648. [PubMed: 11948724]

26. Zhang S, Merritt M, Woessner D, Lenkinski R, Sherry A. PARACEST agents: modulating MRI contrast via water proton exchange. Acc Chem Res. 2003; 36(10):783–790. [PubMed: 14567712]

27. Woods M, Woessner DE, Sherry AD. Paramagnetic lanthanide complexes as PARACEST agents for medical imaging. Chem Soc Rev. 2006; 35:500–511. [PubMed: 16729144]

28. McMahon MT, Gilad AA, DeLiso MA, Berman S, Bulte JWM, van Zijl PCM. New "multicolor" polypeptide diamagnetic chemical exchange saturation transfer (DIACEST) contrast agents for MRI. Magn Reson Med. 2008; 60(4):803–812. [PubMed: 18816830]

29. Olatunde AO, Dorazio SJ, Spernyak JA, Morrow JR. The NiCEST Approach: Nickel(II) ParaCEST MRI Contrast Agents. J Am Chem Soc. 2012; 134(45):18503–18505. [PubMed: 23102112]

30. Liu G, Moake M, Har-el Y-e, Long CM, Chan KWY, Cardona A, Jamil M, Walczak P, Gilad AA, Sgouros G, van Zijl PCM, Bulte JWM, McMahon MT. In vivo multicolor molecular MR imaging using diamagnetic chemical exchange saturation transfer liposomes. Magn Reson Med. 2012; 67(4):1106–1113. [PubMed: 22392814]

31. Flament J, Geffroy F, Medina C, Robic C, Mayer J-F, Mériaux S, Valette J, Robert P, Port M, Le Bihan D, Lethimonnier F, Boumezbeur F. In vivo CEST MR imaging of U87 mice brain tumor angiogenesis using targeted LipoCEST contrast agent at 7 T. Magn Reson Med. 2013; 69(1):179–187. [PubMed: 22378016]

32. Chan KWY, Yu T, Qiao Y, Liu Q, Yang M, Patel H, Liu G, Kinzler KW, Vogelstein B, Bulte JWM, van Zijl PCM, Hanes J, Zhou S, McMahon MT. A diaCEST MRI approach for monitoring liposomal accumulation in tumors. J Control Release. 2014; 180(0):51–59. [PubMed: 24548481]

33. Song X, Yang X, Ray Banerjee S, Pomper MG, McMahon MT. Anthranilic acid analogs as diamagnetic CEST MRI contrast agents that feature an intramolecular-bond shifted hydrogen. Contrast Media Mol Imaging. 2014 n/a-n/a.

34. Tsitovich PB, Spernyak JA, Morrow JR. A Redox-Activated MRI Contrast Agent that Switches Between Paramagnetic and Diamagnetic States. Angew Chem Int Ed Engl. 2013; 52(52):13997–14000. [PubMed: 24222651]

35. Gilad AA, McMahon MT, Walczak P, Winnard PT Jr. Raman V, van Laarhoven HW, Skoglund CM, Bulte JW, van Zijl PC. Artificial reporter gene providing MRI contrast based on proton exchange. Nat Biotechnol. 2007; 25(2):217–219. [PubMed: 17259977]

36. Vasalatiy O, Gerard RD, Zhao P, Sun X, Sherry AD. Labeling of Adenovirus Particles with PARACEST Agents. Bioconjug Chem. 2008; 19(3):598–606. [PubMed: 18254605]

37. Chan KWY, Liu G, Song X, Kim H, Yu T, Arifin DR, Gilad AA, Hanes J, Walczak P, van Zijl PCM, Bulte JWM, McMahon MT. MRI-detectable pH nanosensors incorporated into hydrogels for in vivo sensing of transplanted-cell viability. Nat Mater. 2013; 12(3):268–275. [PubMed: 23353626]

38. Liu G, Bettegowda C, Qiao Y, Staedtke V, Chan KWY, Bai R, Li Y, Riggins GJ, Kinzler KW, Bulte JWM, McMahon MT, Gilad AA, Vogelstein B, Zhou S, van Zijl PCM. Noninvasive imaging of infection after treatment with tumor-homing bacteria using Chemical Exchange Saturation Transfer (CEST) MRI. Magn Reson Med. 2013; 70(6):1690–1698. [PubMed: 24123389]

39. Liu Q, Tawackoli W, Pelled G, Fan Z, Jin N, Natsuaki Y, Bi X, Gart A, Bae H, Gazit D, Li D. Detection of low back pain using pH level-dependent imaging of the intervertebral disc using the ratio of R1ρ dispersion and −OH chemical exchange saturation transfer (RROC). Magn Reson Med. 2014 in press.

40. McVicar N, Li AX, Suchý M, Hudson RHE, Menon RS, Bartha R. Simultaneous in vivo pH and temperature mapping using a PARACEST-MRI contrast agent. Magn Reson Med. 2013; 70(4):1016–1025. [PubMed: 23165779]

41. Huang Y, Coman D, Ali MM, Hyder F. Lanthanide ion (III) complexes of 1,4,7,10-tetraazacyclododecane-1,4,7,10-tetraaminophosphonate for dual biosensing of pH with chemical exchange saturation transfer (CEST) and biosensor imaging of redundant deviation in shifts (BIRDS). Contrast Media Mol Imaging. 2014 n/a-n/a.

42. Zhou J, Payen JF, Wilson DA, Traystman RJ, van Zijl PC. Using the amide proton signals of intracellular proteins and peptides to detect pH effects in MRI. Nat Med. 2003; 9(8):1085–1090. [PubMed: 12872167]

43. Zhou J, Tryggestad E, Wen Z, Lal B, Zhou T, Grossman R, Wang S, Yan K, Fu D-X, Ford E, Tyler B, Blakeley J, Laterra J, van Zijl PCM. Differentiation between glioma and radiation necrosis using molecular magnetic resonance imaging of endogenous proteins and peptides. Nat Med. 2011; 17(1):130–134. [PubMed: 21170048]

44. Guivel-Scharen V, Sinnwell T, Wolff SD, Balaban RS. Detection of Proton Chemical Exchange between Metabolites and Water in Biological Tissues. J Magn Reson. 1998; 133(1):36–45. [PubMed: 9654466]

45. Sun PZ, Cheung JS, Wang EF, Lo EH. Association between pH-weighted endogenous amide proton chemical exchange saturation transfer MRI and tissue lactic acidosis during acute ischemic stroke. J Cereb Blood Flow Metab. 2011; 31(8):1743–1750. [PubMed: 21386856]

46. Sun PZ, Zhou J, Sun W, Huang J, van Zijl PC. Detection of the ischemic penumbra using pH-weighted MRI. J Cereb Blood Flow Metab. 2007; 27(6):1129–1136. [PubMed: 17133226]

47. Jin T, Wang P, Zong X, Kim S-G. MR imaging of the amide-proton transfer effect and the pH-insensitive nuclear overhauser effect at 9.4 T. Magn Reson Med. 2013; 69(3):760–770. [PubMed: 22577042]

48. Zhou J, van Zijl PCM. Chemical Exchange Saturation Transfer Imaging. Prog Nucl Magn Reson Spectrosc. 2006; 48:109–136.

49. Sun PZ, Wang Y, Xiao G, Wu R. Simultaneous experimental determination of labile proton fraction ratio and exchange rate with irradiation radio frequency power-dependent quantitative CEST MRI analysis. Contrast Media Mol Imaging. 2013; 8(3):246–251. [PubMed: 23606428]

50. Sun PZ. Simultaneous determination of labile proton concentration and exchange rate utilizing optimal RF power: radio frequency power (RFP) dependence of chemical exchange saturation transfer (CEST) MRI. J Magn Reson. 2010; 202(2):155–161. [PubMed: 19926319]

51. Sun PZ, Lu J, Wu Y, Xiao G, Wu R. Evaluation of the dependence of CEST-EPI measurement on repetition time, RF irradiation duty cycle and imaging flip angle for enhanced pH sensitivity. Phys Med Biol. 2013; 58:N229–N240. [PubMed: 23939228]

52. Murase K, Tanki N. Numerical solutions to the time-dependent Bloch equations revisited. Magn Reson Imaging. 2011; 29(1):126–131. [PubMed: 20832224]

53. Zhou J, Wilson DA, Sun PZ, Klaus JA, van Zijl PCM. Quantitative description of proton exchange processes between water and endogenous and exogenous agents for WEX, CEST, and APT experiments. Magn Reson Med. 2004; 51(5):945–952. [PubMed: 15122676]

54. Woessner DE, Zhang S, Merritt ME, Sherry AD. Numerical solution of the Bloch equations provides insights into the optimum design of PARACEST agents for MRI. Magn Reson Med. 2005; 53(4):790–799. [PubMed: 15799055]

55. Sun PZ, Sorensen AG. Imaging pH using the chemical exchange saturation transfer (CEST) MRI: correction of concomitant RF irradiation effects to quantify CEST MRI for chemical exchange rate and pH. Magn Reson Med. 2008; 60(2):390–397. [PubMed: 18666128]

56. Li AX, Hudson RHE, Barrett JW, Johns CK, Pasternak SH, Bartha R. Four-pool modeling of proton exchange processes in biological systems in the presence of MRI-paramagnetic chemical exchange saturation transfer (PARACEST) agents. Magn Reson Med. 2008; 60(5):1197–1206. [PubMed: 18958857]

57. Chen JH, Sambol EB, DeCarolis P, O'Connor R, Geha RC, Wu YV, Singer S. High-resolution MAS NMR spectroscopy detection of the spin magnetization exchange by cross-relaxation and chemical exchange in intact cell lines and human tissue specimens. Magn Reson Med. 2006; 55(6):1246–1256. [PubMed: 16676334]

58. Avni R, Mangoubi O, Bhattacharyya R, Degani H, Frydman L. Magnetization transfer magic-angle-spinning z-spectroscopy of excised tissues. J Magn Reson. 2009; 199(1):1–9. [PubMed: 19409825]
59. Friedman JI, McMahon MT, Stivers JT, Van Zijl PCM. Indirect Detection of Labile Solute Proton Spectra via the Water Signal Using Frequency-Labeled Exchange (FLEX) Transfer. J Am Chem Soc. 2010; 132(6):1813–1815. [PubMed: 20095603]
60. Sun PZ. Simplified and scalable numerical solution for describing multi-pool chemical exchange saturation transfer (CEST) MRI contrast. J Magn Reson. 2010; 205(2):235–241. [PubMed: 20570196]
61. Horska A, Spencer GS. Correctly accounting for radiofrequency spillover in saturation transfer experiments: application to measurement of the creatine kinase reaction rate in human forearm muscle. MAGMA. 1997; 5(2):159–163. [PubMed: 9268080]
62. Baguet E, Roby C. Off-resonance irradiation effect in steady-state NMR saturation transfer. J Magn Reson. 1997; 128(2):149–160. [PubMed: 9356270]
63. Sun PZ, van Zijl PCM, Zhou J. Optimization of the irradiation power in chemical exchange dependent saturation transfer experiments. J Magn Reson. 2005; 175(2):193–200. [PubMed: 15893487]
64. Zaiss M, Schmitt B, Bachert P. Quantitative separation of CEST effect from magnetization transfer and spillover effects by Lorentzian-line-fit analysis of z-spectra. J Magn Reson. 2011; 211(2):149–155. [PubMed: 21641247]
65. Jones CK, Polders D, Hua J, Zhu H, Hoogduin HJ, Zhou J, Luijten P, van Zijl PCM. In vivo three-dimensional whole-brain pulsed steady-state chemical exchange saturation transfer at 7 T. Magn Reson Med. 2012; 67(6):1579–1589. [PubMed: 22083645]
66. Desmond KL, Moosvi F, Stanisz GJ. Mapping of amide, amine, and aliphatic peaks in the CEST spectra of murine xenografts at 7 T. Magn Reson Med. 2014; 71(5):1841–1853. [PubMed: 23801344]
67. Sheth VR, Li Y, Chen LQ, Howison CM, Flask CA, Pagel MD. Measuring in vivo tumor pHe with CEST-FISP MRI. Magn Reson Med. 2012; 67(3):760–768. [PubMed: 22028287]
68. Jin T, Autio J, Obata T, Kim S-G. Spin-locking versus chemical exchange saturation transfer MRI for investigating chemical exchange process between water and labile metabolite protons. Magn Reson Med. 2011; 65(5):1448–1460. [PubMed: 21500270]
69. Trott O, Palmer AG. R1rho Relaxation outside of the Fast-Exchange Limit. J Magn Reson. 2002; 154(1):157–160. [PubMed: 11820837]
70. Murase K. Behavior of the magnetization in spin-locking magnetic resonance imaging using numerical solutions to the time-dependent Bloch equations. Phys Med Biol. 2012; 57(23):481–492.
71. Jin T, Wang P, Zong X, Kim S-G. Magnetic resonance imaging of the Amine Proton EXchange (APEX) dependent contrast. NeuroImage. 2012; 16(2):1218–1227. [PubMed: 21871570]
72. Zaiss M, Xu J, Goerke S, Khan IS, Singer RJ, Gore JC, Gochberg DF, Bachert P. Inverse Z-spectrum analysis for spillover-, MT-, and T1-corrected steady-state pulsed CEST-MRI – application to pH-weighted MRI of acute stroke. NMR Biomed. 2014; 27(3):240–252. [PubMed: 24395553]
73. Fischer HW, Rinck PA, van Haverbeke Y, Muller RN. Nuclear relaxation of human brain gray and white matter: Analysis of field dependence and implications for MRI. Magn Reson Med. 1990; 16(2):317–334. [PubMed: 2266850]
74. Oros-Peusquens AM, Laurila M, Shah NJ. Magnetic field dependence of the distribution of NMR relaxation times in the living human brain. MAGMA. 2008; 21(1-2):131–147. [PubMed: 18338191]
75. Sun PZ, Zhou J, Huang J, van Zijl P. Simplified quantitative description of amide proton transfer (APT) imaging during acute ischemia. Magn Reson Med. 2007; 57(2):405–410. [PubMed: 17260362]
76. Ali MM, Liu G, Shah T, Flask CA, Pagel MD. Using Two Chemical Exchange Saturation Transfer Magnetic Resonance Imaging Contrast Agents for Molecular Imaging Studies. Acc Chem Res. 2009; 42(7):915–924. [PubMed: 19514717]

77. Wu R, Liu C, Liu P, Sun PZ. Improved measurement of labile proton concentration-weighted chemical exchange rate (kws) with experimental factor-compensated and T1-normalized quantitative chemical exchange saturation transfer (CEST) MRI. Contrast Media Mol Imaging. 2012; 7(4):384–389. [PubMed: 22649044]
78. Sun PZ. Simplified quantification of labile proton concentration-weighted chemical exchange rate (kws) with RF saturation time dependent ratiometric analysis (QUESTRA): Normalization of relaxation and RF irradiation spillover effects for improved quantitative chemical exchange saturation transfer (CEST) MRI. Magn Reson Med. 2012; 67(4):936–942. [PubMed: 21842497]
79. Scheidegger R, Vinogradov E, Alsop DC. Amide proton transfer imaging with improved robustness to magnetic field inhomogeneity and magnetization transfer asymmetry using saturation with frequency alternating RF irradiation. Magn Reson Med. 2011; 66(5):1275–1285. [PubMed: 21608029]
80. Zu Z, Janve VA, Xu J, Does MD, Gore JC, Gochberg DF. A new method for detecting exchanging amide protons using chemical exchange rotation transfer. Magn Reson Med. 2013; 69(3):637–647. [PubMed: 22505325]
81. Gochberg DF, Kennan RP, Roberson PL, Gore JC. Quantitative imaging magnetization transfer multiple selective pulses. Magn Reson Med. 1999; 41:1065–1072. [PubMed: 10332891]
82. Sun PZ, Benner T, Kumar A, Sorensen AG. Investigation of optimizing and translating pH-sensitive pulsed-chemical exchange saturation transfer (CEST) imaging to a 3T clinical scanner. Magn Reson Med. 2008; 60(4):834–841. [PubMed: 18816867]
83. Mougin OE, Coxon RC, Pitiot A, Gowland PA. Magnetization transfer phenomenon in the human brain at 7 T. NeuroImage. 2010; 49(1):272–281. [PubMed: 19683581]
84. Tee YK, Khrapitchev AA, Sibson NR, Payne SJ, Chappell MA. Optimal sampling schedule for chemical exchange saturation transfer. Magn Reson Med. 2013; 70(5):1251–1262. [PubMed: 23315799]
85. Sun PZ, Wang E, Cheung JS, Zhang X, Benner T, Sorensen AG. Simulation and optimization of pulsed radio frequency (RF) irradiation scheme for chemical exchange saturation transfer (CEST) MRI – demonstration of pH-weighted pulsed-amide proton CEST MRI in an animal model of acute cerebral ischemia. Magn Reson Med. 2011; 66(4):1042–1048. [PubMed: 21437977]
86. Zu Z, Li K, Janve VA, Does MD, Gochberg DF. Optimizing pulsed-chemical exchange saturation transfer imaging sequences. Magn Reson Med. 2011; 66(4):1100–1108. [PubMed: 21432903]
87. Schmitt B, Zaiß M, Zhou J, Bachert P. Optimization of pulse train presaturation for CEST imaging in clinical scanners. Magn Reson Med. 2011; 65(6):1620–1629. [PubMed: 21337418]
88. Vinogradov E, Zhang S, Lubag A, Balschi JA, Sherry AD, Lenkinski RE. On-resonance low B1 pulses for imaging of the effects of PARACEST agents. J Magn Reson. 2005; 176(1):54–63. [PubMed: 15979362]
89. Keupp, J.; Baltes, C.; Harver, P.; Van den Brink, J. Parallel RF Transmission based MRI Technique for Highly Sensitive Detection of Amide Proton Transfer in the Human Brain at 3T.. ISMRM 19th Annual Meeting & Exhibition; Montréal, Québec, Canada. 2011; p. 710
90. Sun PZ, Murata Y, Lu J, Wang X, Lo EH, Sorensen AG. Relaxation-compensated fast multislice amide proton transfer (APT) imaging of acute ischemic stroke. Magn Reson Med. 2008; 59(5): 1175–1182. [PubMed: 18429031]
91. Sun PZ, Cheung JS, Wang E, Benner T, Sorensen AG. Fast multi-slice pH-weighted chemical exchange saturation transfer (CEST) MRI with unevenly segmented RF irradiation. Magn Reson Med. 2011; 65(2):588–594. [PubMed: 20872859]
92. Sun PZ, Wang Y, Lu J. Sensitivity-enhanced chemical exchange saturation transfer (CEST) MRI with least squares optimization of Carr Purcell Meiboom Gill multi-echo echo planar imaging. Contrast Media Mol Imaging. 2014; 9(2):177–181. [PubMed: 24523063]
93. Liu G, Ali MM, Yoo B, Griswold MA, Tkach JA, Pagel MD. PARACEST MRI with improved temporal resolution. Magn Reson Med. 2009; 61(2):399–408. [PubMed: 19165903]
94. Zhu H, Jones CK, van Zijl PCM, Barker PB, Zhou J. Fast 3D chemical exchange saturation transfer (CEST) imaging of the human brain. Magn Reson Med. 2010; 64(3):638–644. [PubMed: 20632402]

95. Shah T, Lu L, Dell KM, Pagel MD, Griswold MA, Flask CA. CEST-FISP: A novel technique for rapid chemical exchange saturation transfer MRI at 7 T. Magn Reson Med. 2011; 65(2):432–437. [PubMed: 20939092]

96. Dopfert J, Zaiss M, Witte C, Schroder L. Ultrafast CEST imaging. J Magn Reson. 2013; 243(0): 47–53. [PubMed: 24721681]

97. Xiao, G.; Sun, PZ.; Dai, Z.; Wu, R. Preliminary Evaluation of Compress Sensing Chemical Exchange Saturation Transfer (CEST) MRI.. Joint Annual Meeting ISMRM-ESMRMB; Milan, Italy. 2014; p. 3297

98. Varma G, Lenkinski RE, Vinogradov E. Keyhole chemical exchange saturation transfer. Magn Reson Med. 2012; 68(4):1228–1233. [PubMed: 22246655]

99. Bhave, S.; Kim, J.; Johnson, C.; Jacob, M. Accelerated CEST MRI using compressive sensing and multishot spiral acquisitions.. ISMRM 21st Annual Meeting & Exhibition; Salt Lake City, Utah, USA. 2013; p. 2613

100. McMahon M, Gilad A, Zhou J, Sun PZ, Bulte J, van Zijl PC. Quantifying exchange rates in chemical exchange saturation transfer agents using the saturation time and saturation power dependencies of the magnetization transfer effect on the magnetic resonance imaging signal (QUEST and QUESP): Ph calibration for poly-L-lysine and a starburst dendrimer. Magn Reson Med. 2006; 55(4):836–847. [PubMed: 16506187]

101. Sun PZ, Wang Y, Dai Z, Xiao G, Wu R. Quantitative chemical exchange saturation transfer (qCEST) MRI - RF spillover effect-corrected omega plot for simultaneous determination of labile proton fraction ratio and exchange rate. Contrast Media Mol Imaging. 2014; 9(4):268–275. [PubMed: 24706610]

102. Randtke EA, Chen LQ, Corrales LR, Pagel MD. The Hanes-Woolf linear QUESP method improves the measurements of fast chemical exchange rates with CEST MRI. Magn Reson Med. 2014; 71(4):1603–1612. [PubMed: 23780911]

103. Randtke EA, Chen LQ, Pagel MD. The reciprocal linear QUEST analysis method facilitates the measurements of chemical exchange rates with CEST MRI. Contrast Media Mol Imaging. 2014; 9(3):252–258. [PubMed: 24700753]

104. Zu Z, Janve VA, Li K, Does MD, Gore JC, Gochberg DF. Multi-angle ratiometric approach to measure chemical exchange in amide proton transfer imaging. Magn Reson Med. 2012; 68(3): 711–719. [PubMed: 22161770]

105. Xu J, Zaiss M, Zu Z, Li H, Xie J, Gochberg DF, Bachert P, Gore JC. On the origins of chemical exchange saturation transfer (CEST) contrast in tumors at 9.4T. NMR Biomed. 2014; 27(4):406–416. [PubMed: 24474497]

106. Dixon TW, Ren J, Lubag A, J. M. Ratnakar J, Vinogradov E, Hancu I, Lenkinski R,E, Sherry AD. A concentration-independent method to measure exchange rates in PARACEST agents. Magn Reson Med. 2010; 63(3):625–632. [PubMed: 20187174]

107. Zaiss M, Bachert P. Exchange-dependent relaxation in the rotating frame for slow and intermediate exchange – modeling off-resonant spin-lock and chemical exchange saturation transfer. NMR Biomed. 2013; 26(5):507–518. [PubMed: 23281186]

108. Ward KM, Balaban RS. Determination of pH using water protons and chemical exchange dependent saturation transfer (CEST). Magn Reson Med. 2000; 44(5):799–802. [PubMed: 11064415]

109. Sun PZ, Longo DL, Hu W, Xiao G, Wu R. Quantification of iopamidol multi-site chemical exchange properties for ratiometric chemical exchange saturation transfer (CEST) imaging of pH. Phys Med Biol. 2014; 59(16):4493. [PubMed: 25054859]

110. Li Y, Sheth VR, Liu G, Pagel MD. A self-calibrating PARACEST MRI contrast agent that detects esterase enzyme activity. Contrast Media Mol Imaging. 2011; 6(4):219–228. [PubMed: 21861282]

111. Aime S, Calabi L, Biondi L, Miranda MD, Ghelli S, Paleari L, Rebaudengo C, Terreno E. Iopamidol: Exploring the potential use of a well-established x-ray contrast agent for MRI. Magn Reson Med. 2005; 53(4):830–834. [PubMed: 15799043]

112. Longo DL, Busato A, Lanzardo S, Antico F, Aime S. Imaging the pH evolution of an acute kidney injury model by means of iopamidol, a MRI-CEST pH-responsive contrast agent. Magn Reson Med. 2012; 70(3):859–864. [PubMed: 23059893]

113. Longo DL, Dastrù W, Digilio G, Keupp J, Langereis S, Lanzardo S, Prestigio S, Steinbach O, Terreno E, Uggeri F, Aime S. Iopamidol as a responsive MRI-chemical exchange saturation transfer contrast agent for pH mapping of kidneys: In vivo studies in mice at 7 T. Magn Reson Med. 2011; 65(1):202–211. [PubMed: 20949634]

114. Chen LQ, Howison CM, Jeffery JJ, Robey IF, Kuo PH, Pagel MD. Evaluations of extracellular pH within in vivo tumors using acidoCEST MRI. Magn Reson Med. 2013 in press.

115. McVicar N, Li AX, Goncalves DF, Bellyou M, Meakin SO, Prado MAM, Bartha R. Quantitative tissue pH measurement during cerebral ischemia using amine and amide concentration-independent detection (AACID) with MRI. J Cereb Blood Flow Metab. 2014; 34(4):690–698. [PubMed: 24496171]

116. Henkelman RM, Stanisz GJ, Graham SJ. Magnetization transfer in MRI: a review. NMR Biomed. 2001; 14:57–64. [PubMed: 11320533]

117. Ewing JR, Jiang Q, Boska M, Zhang ZG, Brown SL, Li GH, Divine GW, Chopp M. T_1 and magnetization transfer at 7 Tesla in acute ischemic infarct in the rat. Magn Reson Med. 1999; 41(4):696–705. [PubMed: 10332844]

118. Balaban RS, Ceckler TL. Magnetization transfer contrast in magnetic resonance imaging. Magn Reson Q. 1992; 8:116–137. [PubMed: 1622774]

119. Ropele S, Filippi M, Valsasina P, Korteweg T, Barkhof F, Tofts PS, Samson R, Miller DH, Fazekas F. Assessment and correction of B1-induced errors in magnetization transfer ratio measurements. Magn Reson Med. 2005; 53(1):134–140. [PubMed: 15690512]

120. Samson RS, Wheeler-Kingshott CAM, Symms MR, Tozer DJ, Tofts PS. A simple correction for B1 field errors in magnetization transfer ratio measurements. Magn Reson Imaging. 2006; 24(3): 255–263. [PubMed: 16563954]

121. Henkelman RM, Huang X, Xiang Q-S, Stanisz GJ, Swanson SD, Bronskill MJ. Quantitative interpretation of magnetization transfer. Magn Reson Med. 1993; 29:759–766. [PubMed: 8350718]

122. Wei W, Jia G, Flanigan D, Zhou J, Knopp MV. Chemical exchange saturation transfer MR imaging of articular cartilage glycosaminoglycans at 3T: Accuracy of B0 Field Inhomogeneity corrections with gradient echo method. Magn Reson Imaging. 2014; 32(1):41–47. [PubMed: 24119460]

123. Dula AN, Arlinghaus LR, Dortch RD, Dewey BE, Whisenant JG, Ayers GD, Yankeelov TE, Smith SA. Amide proton transfer imaging of the breast at 3 T: Establishing reproducibility and possible feasibility assessing chemotherapy response. Magn Reson Med. 2013; 70(1):216–224. [PubMed: 22907893]

124. Kim M, Gillen J, Landman BA, Zhou J, van Zijl PCM. Water saturation shift referencing (WASSR) for chemical exchange saturation transfer (CEST) experiments. Magn Reson Med. 2009; 61(6):1441–1450. [PubMed: 19358232]

125. Song, X.; Chan, KY.; McMahon, M. Screening of CEST MR Contrast Agents.. In: Schröder, L.; Faber, C., editors. In vivo NMR Imaging. Volume 771, Methods in Molecular Biology. Humana Press; 2011. p. 171-187.

126. Zhou J, Blakeley JO, Hua J, Kim M, Laterra J, Pomper MG, van Zijl PCM. Practical data acquisition method for human brain tumor amide proton transfer (APT) imaging. Magn Reson Med. 2008; 60(4):842–849. [PubMed: 18816868]

127. Song X, Gilad AA, Joel S, Liu G, Bar-Shir A, Liang Y, Gorelik M, Pekar JJ, van Zijl PCM, Bulte JWM, McMahon MT. CEST phase mapping using a length and offset varied saturation (LOVARS) scheme. Magn Reson Med. 2012; 68(4):1074–1086. [PubMed: 22246684]

128. Liu G, Chan KWY, Song X, Zhang J, Gilad AA, Bulte JWM, van Zijl PCM, McMahon MT. NOrmalized MAgnetization Ratio (NOMAR) filtering for creation of tissue selective contrast maps. Magn Reson Med. 2013; 69(2):516–523. [PubMed: 22499503]

129. Sun PZ, Zhou J, Sun W, Huang J, van Zijl PCM. Suppression of lipid artifacts in amide proton transfer imaging. Magn Reson Med. 2005; 54(1):222–225. [PubMed: 15968669]

130. Lu J, Zhou J, Cai C, Cai S, Chen Z. Observation of true and pseudo NOE signals using CEST-MRI and CEST-MRS sequences with and without lipid suppression. Magn Reson Med. 2014 in press.

131. Jia G, Abaza R, Williams JD, Zynger DL, Zhou J, Shah ZK, Patel M, Sammet S, Wei L, Bahnson RR, Knopp MV. Amide proton transfer MR imaging of prostate cancer: A preliminary study. J Magn Reson Imaging. 2011; 33(3):647–654. [PubMed: 21563248]

132. Jones CK, Schlosser MJ, van Zijl PCM, Pomper GM, Golay X, Zhou J. Amide proton transfer imaging of human brain tumors at 3T. Magn Reson Med. 2006; 56(3):585–592. [PubMed: 16892186]

133. Dula AN, Asche EM, Landman BA, Welch EB, Pawate S, Sriram S, Gore JC, Smith SA. Development of chemical exchange saturation transfer at 7T. Magn Reson Med. 2012; 66(3): 831–838. [PubMed: 21432902]

134. Sagiyama K, Mashimo T, Togao O, Vemireddy V, Hatanpaa KJ, Maher EA, Mickey BE, Pan E, Sherry AD, Bachoo RM, Takahashi M. In vivo chemical exchange saturation transfer imaging allows early detection of a therapeutic response in glioblastoma. Proc Natl Acad Sci U S A. 2014; 111(12):4542–4547. [PubMed: 24616497]

135. Tietze A, Blicher J, Mikkelsen IK, Østergaard L, Strother MK, Smith SA, Donahue MJ. Assessment of ischemic penumbra in patients with hyperacute stroke using amide proton transfer (APT) chemical exchange saturation transfer (CEST) MRI. NMR Biomed. 2014; 27(2):163–174. [PubMed: 24288260]

136. Togao O, Yoshiura T, Keupp J, Hiwatashi A, Yamashita K, Kikuchi K, Suzuki Y, Suzuki SO, Iwaki T, Hata N, Mizoguchi M, Yoshimoto K, Sagiyama K, Takahashi M, Honda H. Amide proton transfer imaging of adult diffuse gliomas: correlation with histopathological grades. Neuro Oncol. 2014; 16(3):441–448. [PubMed: 24305718]

137. Desmond KL, Stanisz GJ. Understanding quantitative pulsed CEST in the presence of MT. Magn Reson Med. 2012; 67(4):979–990. [PubMed: 21858864]

138. Liu D, Zhou J, Xue R, Zuo Z, An J, Wang DJJ. Quantitative characterization of nuclear overhauser enhancement and amide proton transfer effects in the human brain at 7 tesla. Magn Reson Med. 2013; 70(4):1070–1081. [PubMed: 23238951]

139. Jones CK, Huang A, Xu J, Edden RAE, SchÃ¤r M, Hua J, Oskolkov N, ZacÃ D, Zhou J, McMahon MT, Pillai JJ, van Zijl PCM. Nuclear Overhauser enhancement (NOE) imaging in the human brain at 7 T. NeuroImage. 2013; 77(0):114–124. [PubMed: 23567889]

140. Zhou J, Hong X, Zhao X, Gao J-H, Yuan J. APT-weighted and NOE-weighted image contrasts in glioma with different RF saturation powers based on magnetization transfer ratio asymmetry analyses. Magn Reson Med. 2013; 70(2):320–327. [PubMed: 23661598]

141. Jing Y, Qinwei Z, Yi-Xiang W, Juan W, Jinyuan Z. Accuracy and uncertainty of asymmetric magnetization transfer ratio quantification for amide proton transfer (APT) imaging at 3T: A Monte Carlo study. Jul 3-7.2013 :5139–5142. 2013.

142. Zong X, Wang P, Kim S-G, Jin T. Sensitivity and Source of Amine-Proton Exchange and Amide-Proton Transfer Magnetic Resonance Imaging in Cerebral Ischemia. Magn Reson Med. 2014; 71(1):118–132. [PubMed: 23401310]

143. Makela HI, Kettunen MI, Grohn OH, Kauppinen RA. Quantitative $T_{1\rho}$ and magnetic transfer magnetic resonance imaging of acute cerebral ischemia in the rat. J Cereb Blood Flow Metab. 2002; 22:547–558. [PubMed: 11973427]

144. Jokivarsi KT, Gröhn HI, Gröhn OH, Kauppinen RA. Proton transfer ratio, lactate, and intracellular pH in acute cerebral ischemia. Magn Reson Med. 2007; 57(4):647–653. [PubMed: 17390356]

145. Sun PZ, Wang E, Cheung JS. Imaging acute ischemic tissue acidosis with pH-sensitive endogenous amide proton transfer (APT) MRI – Correction of tissue relaxation and concomitant RF irradiation effects toward mapping quantitative cerebral tissue pH. Neuroimage. 2012; 60(1): 1–6. [PubMed: 22178815]

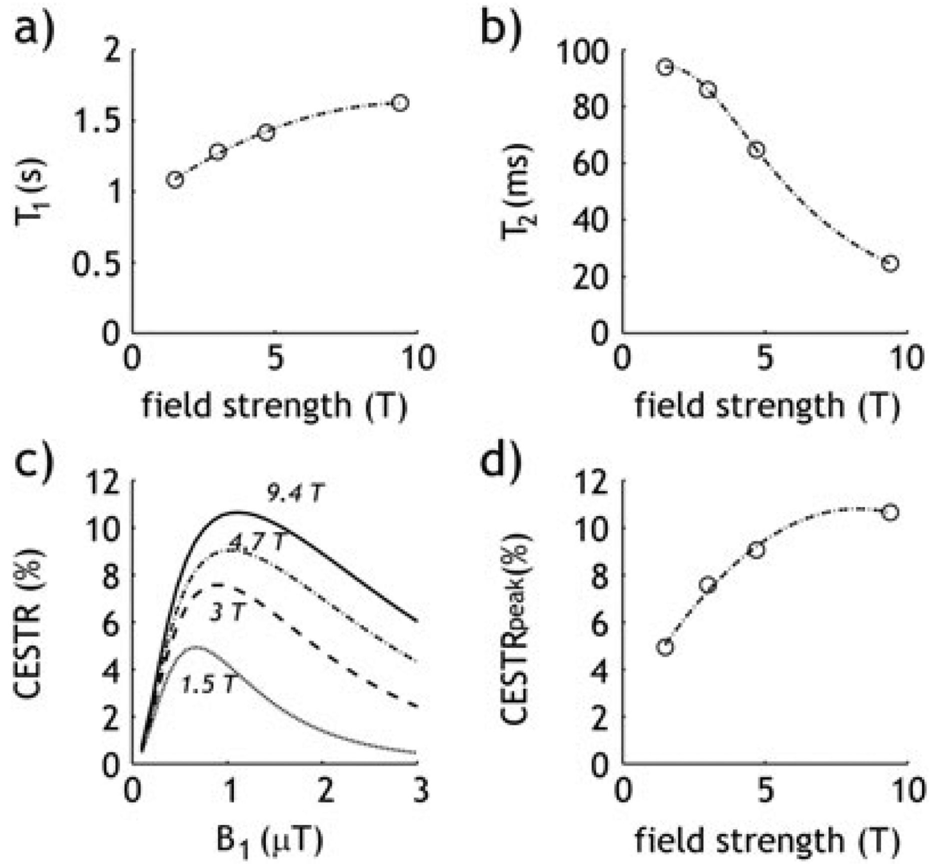

Fig. 1.

Plot of T_1 (a) and T_2 (b) as a function of field strength in grey matter (GM). Simulated CEST effect (CESTR) as a function of B_1 irradiation power (c), and the maximal CEST effect for a given field strength (d).

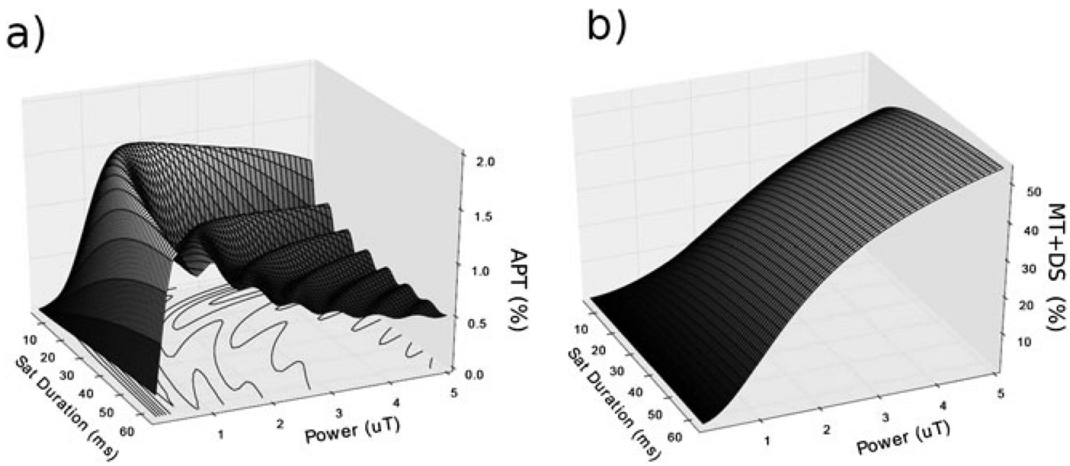

Fig. 2.

(a) APTR effect, and (b) MTC and DS as a function of RF saturation strength and duration for a three-compartment model of semisolid macromolecular protons, solute amide protons, and bulk water protons.

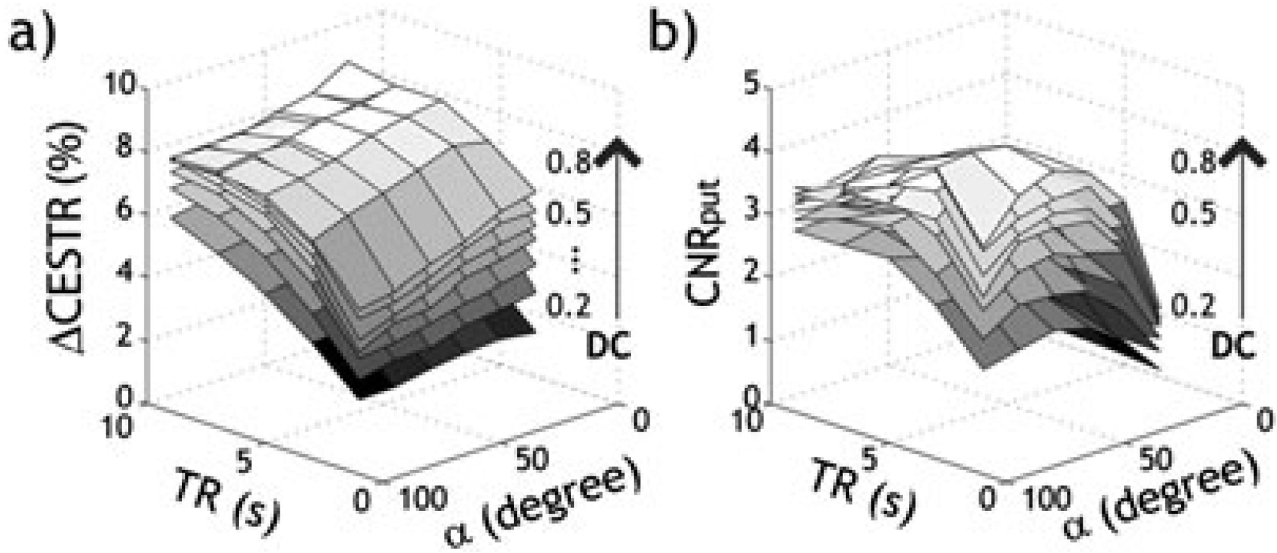

Fig. 3.

Experimental validation of optimal experimental condition in an *in vitro* pH CEST phantom. The pH-weighted CEST contrast (ΔCESTR) increases with TR (a), while its contrast-to-noise ratio efficiency (CNR_{put}) peaks at an intermediate TR (b). Both ΔCESTR (a) and CNR_{put} (b) increase with RF duty cycle. In addition, ΔCESTR decreases with RF flip angle (a), while CNR_{put} initially increased with RF flip angle and peaked at about 75° (b).

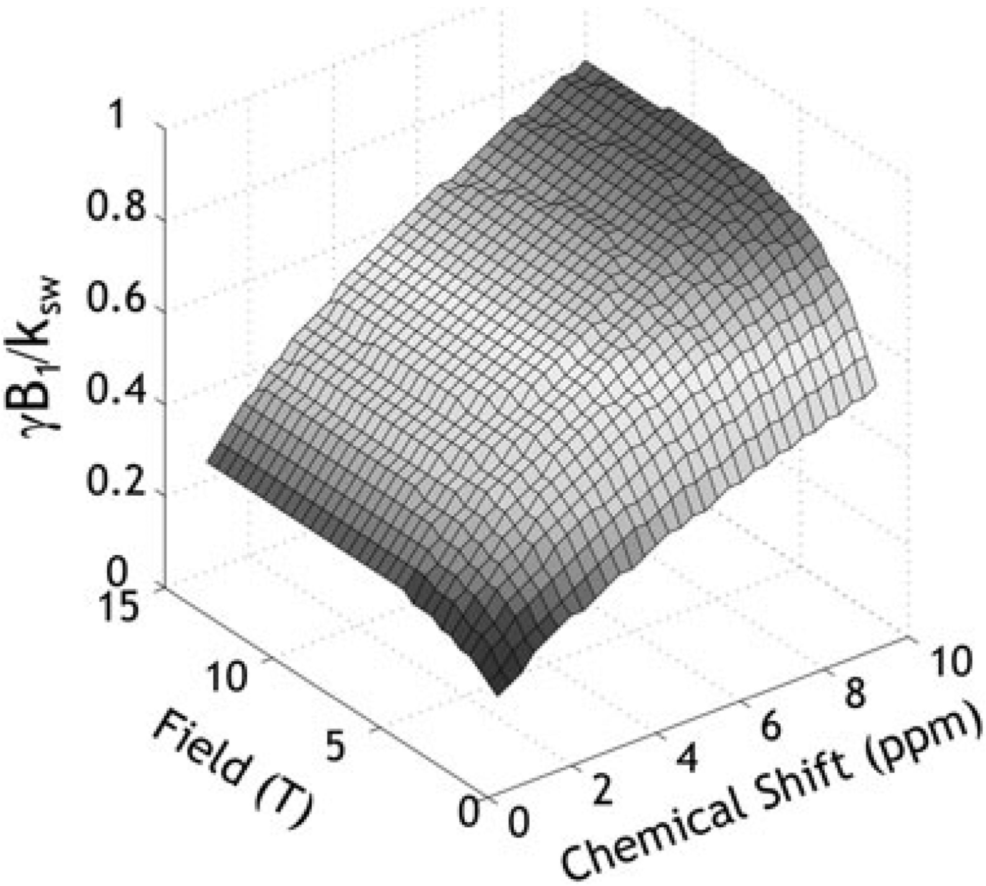

Fig. 4.

Numerically determined optimal B_1 level as a function of field strength and chemical shift. The exchange rate normalized optimal B_1 level approaches unit at high field and chemical shift due to mitigated RF spillover effects.

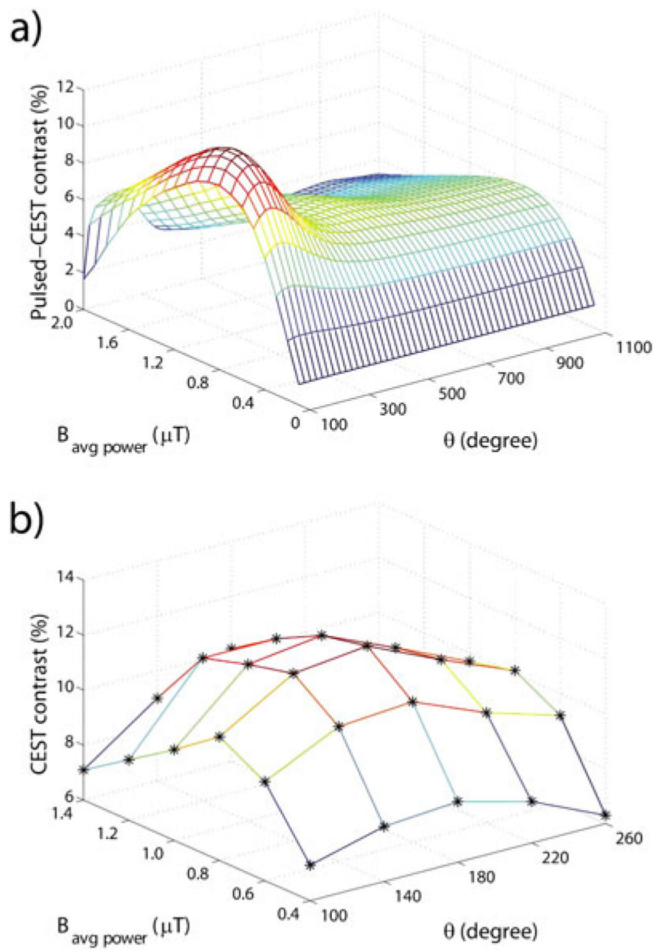

Fig. 5.

(a) Simulated and (b) experimental pulsed-CEST contrast as a function of average power and flip angle of pulsed irradiation at 9.4T with a duty cycle of 50%. Stars represent the experimental results.

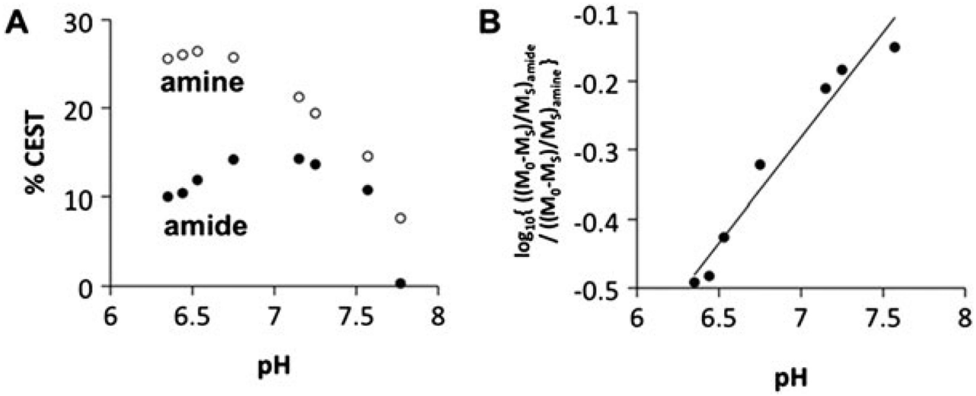

Fig. 6.

CEST ratio-pH correlation for Yb-DO3A-oAA at 300 MHz magnetic field strength. (a) The % CEST effects of the amide (filled circles) and amine (unfilled circles) of 100 mM Yb-DO3A-oAA were measured at 37 °C using 20 μT saturation power. (b) The log10 of a ratio of CEST showed an excellent correlation with pH ($R^2 = 0.99$).

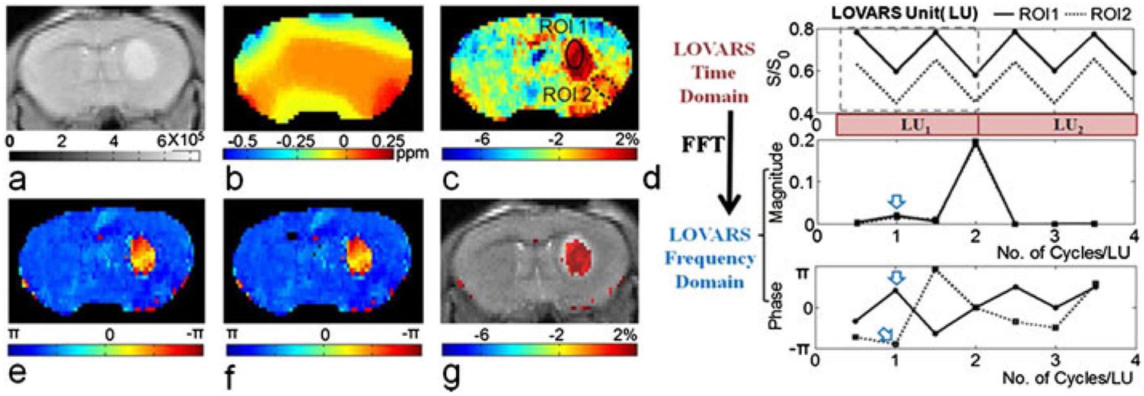

Fig. 7.

In vivo demonstration of the LOVARS scheme as applied to the imaging of 9L gliosarcomas in mice. (a) T2-weighted image; (b) B_0 shift map; (c) uncorrected MTR_{asym} map; (d) LOVARS time domain data (top) with phase (middle) and magnitude (bottom) traces determined through FFT with ROIs as marked in (c); (e) LOVARS phase map calculated using FFT; (f) LOVARS phase map calculated using GLM; (g) thresholded LOVARS imaginary component map.

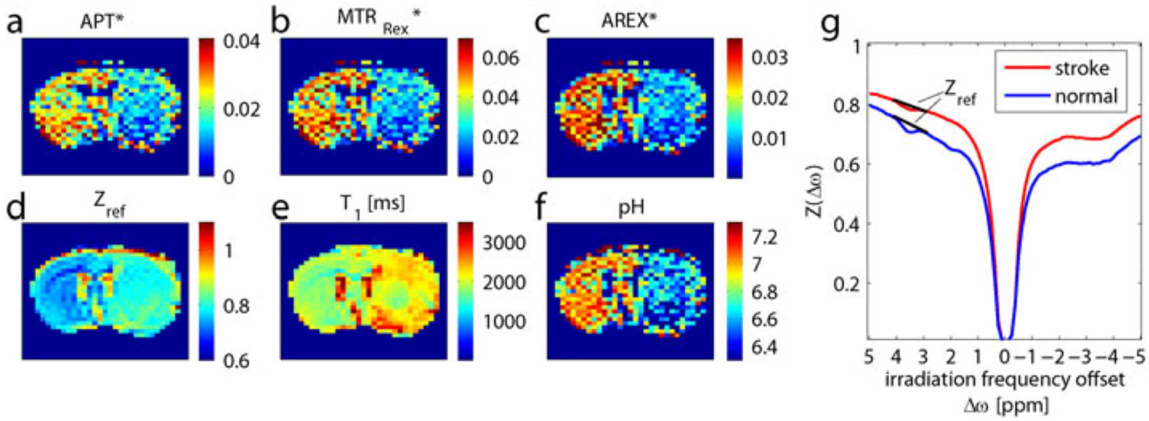

Fig. 8.

(a) Conventional APT contrast is contaminated by (d) spillover and (e) T_1 effects. With correction of spillover by (b) MTR_{Rex} and correction of T_1 by the (c) AREX evaluation, (f) an absolute pH map can be calculated, which shows (g) significantly higher contrast between the stroke area and normal tissue.